Estimates of Regional Source Contributions to the Asian Tropopause Aerosol Layer Using a Chemical Transport Model

T. Duncan Fairlie[1] , Hongyu Liu[2] , Jean-Paul Vernier[2] , Pedro Campuzano-Jost[3] , Jose L. Jimenez[3] , Duseong S. Jo[3] , Bo Zhang[2] , Murali Natarajan[1] , Melody A. Avery[1] , and Gregory Huey[4]

[1]NASA Langley Research Center, Hampton, VA, USA, [2]National Institute of Aerospace, Hampton, VA, USA, [3]Department of Chemistry and Cooperative Institute for Research in Environmental Sciences (CIRES), University of Colorado, Boulder, CO, USA, [4]School of Earth and Atmospheric Sciences, Georgia Institute of Technology, Atlanta, GA, USA

Abstract The Asian Tropopause Aerosol Layer (ATAL) represents an accumulation of aerosol in the upper troposphere and lower stratosphere associated with the Asian Summer Monsoon. Here we simulate the ATAL for summer 2013 with the GEOS-Chem chemical transport model and explore the likely composition of ATAL aerosols and the relative contributions of regional anthropogenic sources versus those from farther afield. The model indicates significant contributions from organic aerosol, nitrate, sulfate, and ammonium aerosol, with regional anthropogenic precursor sources dominant. The model underestimates aerosol backscatter in the ATAL during summer 2013, compared with Cloud-Aerosol Lidar and Infrared Pathfinder Satellite Observations (CALIPSO) satellite instrument. Tests of a more physically based treatment of wet scavenging of SO_2 in convective updrafts raise sulfate, eliminating the low bias with respect to CALIPSO backscatter in the ATAL, but lead to an unacceptable high bias of sulfate compared with in situ observations from aircraft over the United States. Source apportionment of the model results indicate the dominance of regional anthropogenic emissions from China and the Indian subcontinent to aerosol concentrations in the ATAL; ~60% of sulfate in the ATAL region in August 2013 is attributable to anthropogenic sources of SO_2 from China (~30%) and from the Indian subcontinent (~30%), twice as much as in previously published estimates. Nitrate aerosol is found to be a dominant component of aerosol composition on the southern flank of the Asian Summer Monsoon anticyclone. Lightning sources of NO_x are found to make a significant (10–15%) contribution to nitrate in the ATAL for the case studied.

1. Introduction

Satellite observations and modeling studies have indicated that deep convection in the Asian Summer Monsoon (ASM) can serve as a conduit for the transport of gas-phase boundary layer (BL) pollutants (e.g., CO, HCN, CH_4) to the upper troposphere and lower stratosphere (UTLS) (Bergman et al., 2013; Park et al., 2007; Randel et al., 2010; Randel & Park, 2006). The pollutants can accumulate under closed anticyclonic flow conditions, associated with anomalies of low potential vorticity, which characterize the UTLS over much of South Asia during the ASM; strong gradients in potential vorticity along the subtropical jet on the northern flank, and tropical easterlies on the southern side, serve to inhibit exchange of air between inside and outside the region of anticyclonic flow (hereafter, the ASM anticyclone) (Fairlie et al., 2014; Ploeger et al., 2015). However, air is readily detrained east and west from the region due to transience in the flanking jet streams. Specifically, vortex shedding and filamentation associated with Rossby wave breaking along the subtropical jet can lead to dispersion of air masses eastward and irreversible exchange of air with the extratropical lower stratosphere (Vogel et al., 2016). Meanwhile, detrainment into easterly flow in the tropical upper troposphere can lead to dispersion of air masses westward and subsequent diabatic ascent into the tropical lower stratosphere (Garny & Randel, 2016).

Satellite measurements have revealed a coincident peak in aerosol between ~13 and 18 km in the ASM anticyclone. The Asian Tropopause Aerosol Layer (ATAL) was first revealed in CALIOP lidar observations (Vernier et al., 2011) and subsequently detected in SAGE II satellite data from the late 1990s (Thomason
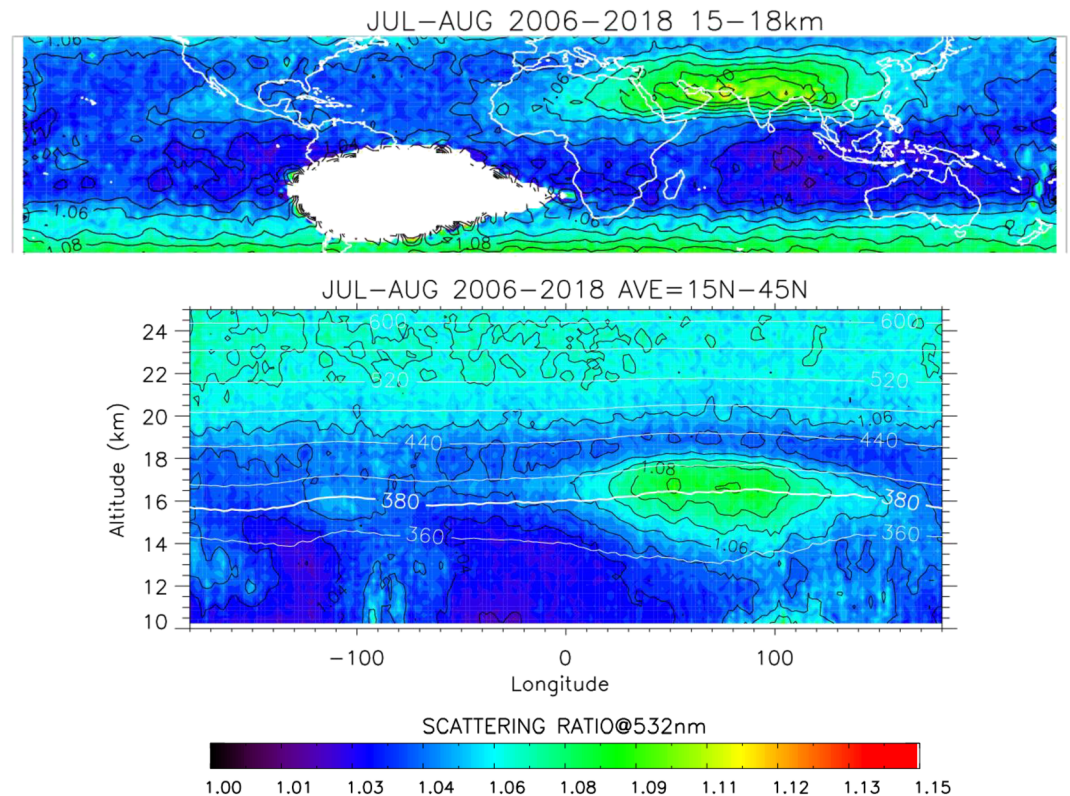
Figure 1. (top panel) Map of cloud-filtered aerosol scattering ratio (SR) from CALIOP between 15 and 18 km averaged for July–August between 2006 and 2018, during periods unaffected by volcanic activity (excluding 2008, 2009, 2011, and 2015); noisy data from the South Atlantic Anomaly on CALIOP are masked in white. (bottom panel) Longitudinal cross-section averaged over the same period between 15°N and 45°N. White contours show isopleths of mean potential temperature (K).

& Vernier, 2013). Figure 1, adapted from Vernier et al. (2015, hereafter V15), shows the mean spatial characteristics of the ATAL. The figure shows a map of cloud-cleared Scattering Ratio (SR) from CALIOP at 532 nm between 15 and 17 km, averaged in July–August between 2006 and 2017, during periods unaffected by volcanic activity (excluding 2008, 2009, 2011, and 2015). SR is defined by $SR = \frac{\beta_{aero} + \beta_{mol}}{\beta_{mol}}$, where β_{aero} and β_{mol} are the aerosol and molecular backscatter, respectively. Specifically, the CALIOP level 1 v4.01 data are first averaged along the orbit track every 300 profiles to increase the signal-to-noise ratio. Depolarization and SRs are then calculated using CALIOP data and MERRA reanalysis. A threshold of 5% in depolarization ratio is applied below 20 km to remove ice clouds. This simple cloud-clearing approach results in a relatively good agreement (within 25%) between CALIOP and balloon-borne in situ backscatter measurements from the Compact Optical Backscatter Aerosol Detector (COBALD) carried out from China (V15) and during the BATAL project in India and Saudi Arabia (Vernier et al., 2018). Enhanced SR, indicating the presence of aerosols, is found over an area extending between East Asia and North Africa, encompassing India and the Middle East. A cross-section of SR, averaged between 15°N and 45°N (Figure 1, bottom panel) over the same period, reveals ATAL aerosols between potential temperatures of 360 and 420 K in the UTLS, extending westward from the top of monsoon convective outflow (V15). V15 showed in situ backscatter measurements from balloon-borne instruments launched from Tibet which provided independent verification of the CALIPSO observations of the ATAL. Vernier et al. (2018) and Yu et al. (2017) provided additional in situ verification of the ATAL from recent balloon launches in India and Saudi Arabia, and from China, respectively. The presence of an ATAL suggests that the ASM may provide a conduit for aerosols, and/or precursor gases, to reach and be dispersed in the UTLS (Neely et al., 2014; Yu et al., 2017). In addition, the proximity of ATAL aerosols to ice clouds in the ASM anticyclone (Vernier et al., 2018) indicates the potential for ATAL aerosols to alter cloud optical properties (Fadnavis et al., 2013, 2017; Li et al., 2005), which could impact regional climate.

The chemical composition and size distribution of ATAL aerosols remain poorly characterized, due to a dearth of in situ observations. In situ observations from the *Civil Aircraft for the Regular Investigation of the Atmosphere based on an Instrument Container* (CARIBIC) aircraft mission (Martinsson et al., 2014) at altitudes a few kilometers below the ATAL (10–12 km) suggest that the ATAL may comprise a mixture of sulfur and carbonaceous aerosol (V15; Yu et al., 2015). Balloon-borne optical particle counter data indicate that the ATAL is composed of fine mostly nonrefractory aerosol (Vernier et al., 2018). Vernier et al. (2018) used a balloon-borne aerosol impactor, and ion chromatography, to detect inorganic nitrate and mineral cations, in the UTLS above India during the ASM. Sulfate was not found above the 10 ng m^{-3} detection limit of the instrument, and organic or elemental-carbon aerosols were not part of the analysis. Aerosol mass spectrometer data and limb-imaging infrared spectrometer data collected during the 2017 StratoClim airborne campaign also indicate ammonium nitrate to be an important component of the aerosol composition (Höpfner et al., 2019). Some of the StratoClim nitrate could be organic rather than inorganic, given the instrument used (e.g., Farmer et al., 2010). However, ATAL composition remains uncertain. Modeling studies have proposed various combinations of aerosol constituents for the ATAL. Yu et al. (2015) used the Community Earth System Model (CESM1) with the Community Aerosol and Radiation Model for Atmospheres (CARMA) to deduce that the ATAL is composed primarily of surface-emitted and secondary organic aerosols (SOAs) (60%), and sulfate (40%). Fadnavis et al. (2013) used the ECHAM5-HAMMOZ aerosol-chemistry-climate model to deduce an ATAL characterized by sulfate, organic, and black carbon (BC) aerosol, with a significant dust component but nitrate was not included in the simulation. Gu et al. (2016) used the GEOS-Chem chemical transport model (CTM) and found inorganic nitrate aerosol to be the dominant component of the simulated ATAL, which they attributed to conditions favoring gas-aerosol conversion of HNO_3.

In addition to composition, the origin and source attribution of ATAL aerosols remain poorly constrained. Bergman et al. (2013) used Lagrangian trajectory calculations to show that the ASM anticyclone is connected to the BL through a relatively narrow transport conduit, focused on North India and the Tibetan Plateau. V15 used back trajectory calculations to track air masses with elevated CALIOP SR to regions of deep convection; they also deduced North India as a principal source of ATAL aerosols and precursor gases. Höpfner et al. (2019) used aerosol mass spectrometer data and limb-imaging infrared spectrometer data collected during the 2017 StratoClim airborne campaign to indicate that ammonium nitrate is an important component of the ATAL aerosol composition. They connected high levels of ammonia in the upper troposphere to ground sources in North India and Pakistan. Vogel et al. (2015) used a Lagrangian model with inert tracers to connect BL air from the Indian subcontinent and China with the ASM anticyclone. They highlighted intraseasonal changes in principal BL source regions (South and East Asia) associated with variability in the morphology and spatial coverage of the ASM anticyclone. Vogel et al. (2016) used the same model to quantify the role of eddy shedding from ASM anticyclone in subsequent intrusions into the extratropical lower stratosphere.

Composition, origin, and source attribution for the ATAL must account for the lifetime of contributing aerosols and precursor gases with respect to chemical and physical loss mechanisms. Scavenging of pollutants during precipitation in moist convective updrafts, e.g., could substantially reduce the impact of local or regional surface sources. CTMs that represent such processes can offer further guidance here. Neely et al. (2014) conducted a global, sulfur-only simulation with in-cloud production of sulfate omitted, and reproduced many features of the observed ATAL. They concluded that anthropogenic emissions of SO_2 from Chinese and Indian source regions contribute only ~30% of sulfate aerosol in the ATAL, arguing that the lifetime of sulfate in the free troposphere is sufficiently long for transport from beyond East and South Asia to be the largest contributor to the region.

In this paper, we use a CTM (GEOS-Chem) to provide further insight into the composition, origin, and transport pathways of ATAL aerosols. We show simulated distributions of carbonaceous, sulfate, nitrate, and ammonium aerosol in the ATAL, and discuss the distribution of gas-phase ammonia, in reference to spectral measurements made from the MIPAS satellite and aircraft limb IR measurements (Höpfner et al., 2016, 2019). We assess the model's ability to represent aerosol backscatter in the ATAL, in comparison with observations from the CALIPSO satellite (Winker et al., 2010). Comparison of the model results with CALIPSO data, and with in situ SO_2 and sulfate observations made during the 2013 Studies of Emissions,

Atmospheric Composition, Clouds, and Climate Coupling by Regional Surveys (SEAC4RS) airborne campaign over North America led us to conduct sensitivity studies to see if altering the model's parameterization of wet scavenging of SO_2 in convective updrafts could alleviate model biases. Specific to this paper, we show the results of source-elimination studies, providing estimates of the relative contributions of anthropogenic sources from the Indian subcontinent and from China to the ATAL aerosol distribution for summer 2013.

2. Model Description

The GEOS-Chem is a state-of-the-science CTM, which is used to simulate gas-phase and aerosol transport and photochemistry in the troposphere (www.geos-chem.org). Here we use model version v9-02. The aerosol simulation represents organic and BC (Park et al., 2003, Park et al., 2004), sulfate-nitrate-ammonium aerosols (Park et al., 2004), mineral dust (Fairlie et al., 2007; Ridley et al., 2014), and sea salt (Jaegle et al., 2011), treated as an external mixture. We use a factor of 2.1 to convert primary organic carbon simulated by the model to organic aerosol (OA) in the ATAL region. A factor of 2.1 has been used in previous studies of OA using GEOS-Chem (Pai et al., 2019, and references therein), and is close to values obtained from aircraft observations (Hodzic et al., 2019; Schroder et al., 2018). We follow Kim et al. (2015) in using the "Simple" scheme to simulate anthropogenic SOA, as the other schemes in GEOS-Chem greatly underestimate this component (e.g., Shah et al., 2019). This scheme represents emissions of an SOA precursor, tied to emissions of monoterpenes and isoprene, and biomass burning CO, biofuel CO, and fossil fuel CO, using the empirical parameterization of Hodzic and Jimenez (2011). SOA is generated via oxidation of the precursor by OH. For biogenic SOA, we use the volatility set approach (VBS) as implemented by Pye et al. (2010). Initial oxidation of isoprene, monoterpenes, and sesquiterpenes with OH, O_3, and NO_3 are simulated with gas-particle partitioning calculation of lumped semivolatiles. Sulfate is produced in the model via gas-phase reaction of OH with SO_2, and in the aqueous phase by dissolution of SO_2 in cloud water, acid-based dissociation, and oxidation by H_2O_2 and O_3 (Alexander et al., 2009; Park et al., 2004). Gas-particle partitioning of sulfate-nitrate-ammonium aerosols is computed using the ISORROPIA II thermodynamic model (Fountoukis & Nenes, 2007), as implemented in GEOS-Chem by Pye et al. (2010). Aerosol dry deposition uses the standard resistance-in-series scheme of Wesely (1989), implemented by Wang et al. (1998). Aerosol wet deposition is described by Liu et al. (2001) with updates by Wang et al. (2011). In-cloud and below cloud scavenging from large-scale precipitation, and scavenging from convective updrafts (Mari et al., 2000), are represented. Gu et al. (2016) used version 9-01-03 of GEOS-Chem, which does not include the "Simple" SOA scheme, to study the aerosol composition of the ATAL. The representation of aerosol used here is little different, except for SOA. The simulations for 2013 shown here are driven by assimilated meteorological analyses from the NASA Global Modeling and Assimilation Office (GMAO) Modern Era Retrospective analysis for Research and Applications (MERRA; Rienecker et al., 2011), which have been mapped from the native grid (0.667° × 0.5°) to 2.5° by 2° horizontal resolution for input to the GEOS-Chem. Note that the model version used when this study was started can only be driven by MERRA or earlier GEOS series; more recent versions may be driven by the MERRA-2 reanalysis, which shows improved climate over MERRA (Molod et al., 2015).

2.1. Emission Inventories

Fossil fuel emissions are taken from the EDGAR database (Olivier & Berdowski, 2001), with regional options, including the Streets 2006 inventory (Zhang et al., 2009) over South and East Asia and the EPA/NEI 2005 inventory over North America. Biofuel emissions are given by Yevich and Logan (2003), with regional options; carbonaceous aerosol emissions are described by Bond et al. (2007); biogenic emissions are provided by the MEGAN model (Guenther et al., 2012); open biomass burning emissions are taken from a monthly climatology (Duncan et al., 2003); and volcanic SO_2 emissions are provided by the AeroCom project (Diehl et al., data available from www.geos-chem.org).

Figure 2 shows prescribed emissions of anthropogenic SO_2, primary OA (POA), NO, and ammonia in the model for August 2013 for the region [0–60°N, 0–130°E]. The emissions shown comprise contributions from both fossil fuel and biofuel emissions (hereafter referred to as anthropogenic emissions). Open biomass burning emissions are also included in the simulations (see above), but are not included in Figure 2. The maps illustrate marked contributions of POA (converted from primary organic carbon using a factor of 2.1) and aerosol precursor gases (SO_2, NO, NH_3) from the Indian subcontinent and from eastern China.
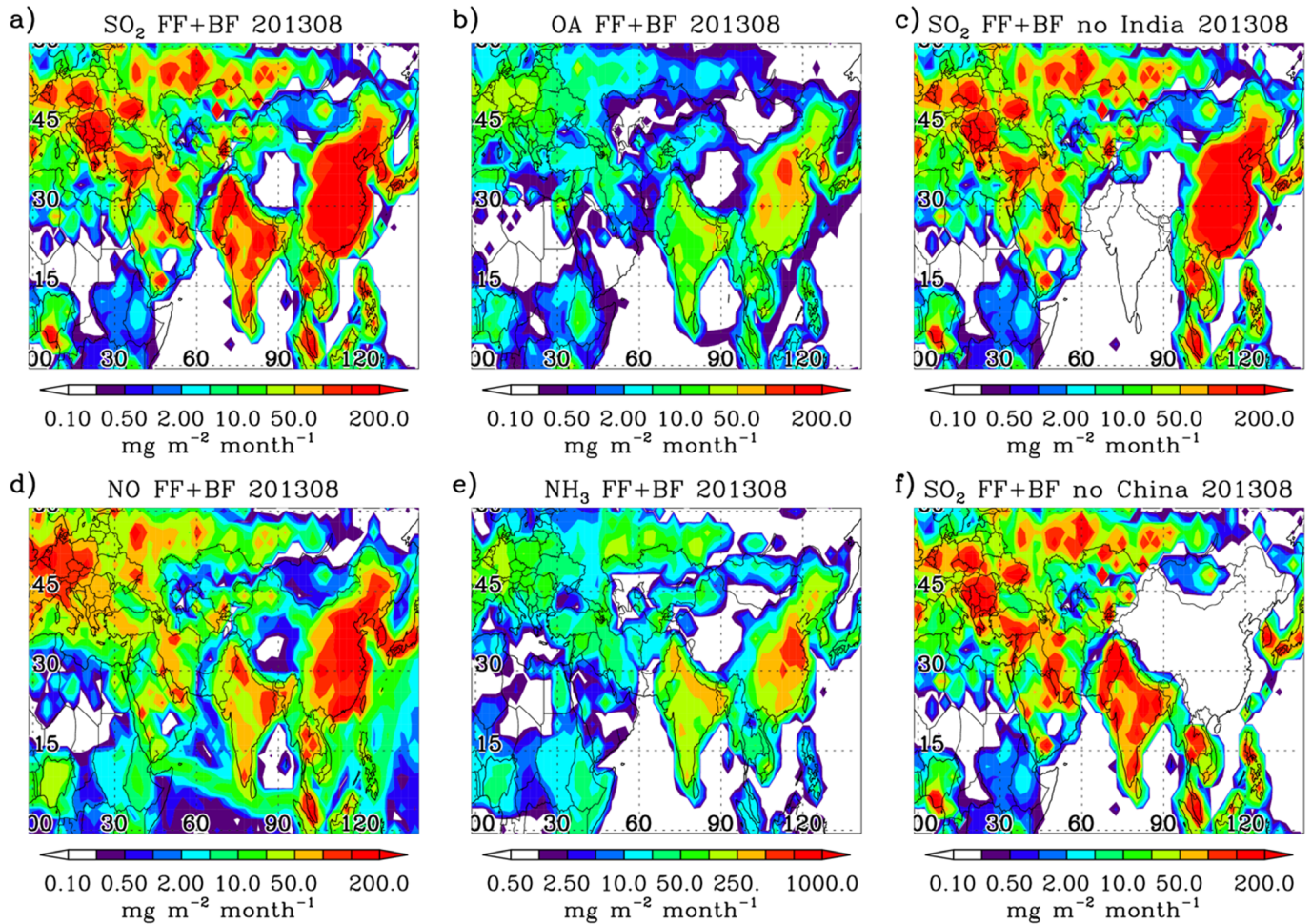
Figure 2. Prescribed anthropogenic emissions of SO$_2$, primary organic aerosol (POA), NO, and ammonia (NH$_3$) for August 2013 (panels a, b, d, and e). Units are mg m^{-2} month^{-1}. Anthropogenic emissions include contributions from both fossil fuel (FF) and biofuel (BF) emissions. Simulations described in this paper include those in which anthropogenic emissions are excluded from the Indian subcontinent ("no-India") and from China ("no-China"), illustrated for SO$_2$ emissions (panels c and f). The former region is defined to include the countries of India, Pakistan, Nepal, Bhutan, Bangladesh, and Sri Lanka.

Emissions of BC (not shown) show a similar distribution to those of POA. Figures 2c and 2f show anthropogenic emissions of SO$_2$ with contributions eliminated from the Indian subcontinent and from China, respectively. Later, we quantify the contributions of these source regions to the ATAL based on simulations that use these source distributions.

2.2. Scavenging in Wet Convective Updrafts

The GEOS-Chem model represents the scavenging of soluble tracers from both large-scale precipitating clouds and in wet convective updrafts (Liu et al., 2001; Mari et al., 2000). The fraction of soluble tracer i lost as air is lifted in convective updrafts by a vertical displacement Δz is given by

$$F_i = 1 - \exp[-k_i \, \Delta z / V_{ud}],$$

where V_{ud} is the updraft velocity (assumed 10 m s^{-1} over land, 5 m s^{-1} over water), and the rate constant, k_i, is given by

$$k_i = (R_i \, f_{iL} + f_{iI}) \, k,$$

where f_{iL} and f_{iI} are the fractions of tracer present in cloud liquid and solid (ice) condensate, respectively; R_i is the retention efficiency of tracer i in liquid cloud condensate as it is converted to precipitation; and k is the

rate of conversion of cloud condensate to precipitation. There are uncertainties in the assumed updraft velocity. However, model simulations of ^{210}Pb aerosols showed little sensitivity to the assumed values due to nearly complete scavenging in deep updrafts (Liu et al., 2001). Most aerosol components in the model, including sulfate-nitrate-ammonium, dust, and sea salt, are assumed 100% in cloud condensate, and subject to wet scavenging. POA and BC are separated into hydrophobic and hydrophilic components at the source of emission (the hydrophobic fractions are 50% for POA, 80% for BC at emission). All SOA is treated as hydrophilic. The hydrophobic components are converted to hydrophilic in the model with an e-folding time of 1.15 days (Cooke et al., 1999). In GEOS-Chem version 9.02, only the hydrophilic parts are subject to wet scavenging except for BC, whose hydrophobic component is subject to scavenging as ice nuclei at temperatures below 258 K (Wang et al., 2011). Scavenging of the sulfate precursor SO_2 follows the scheme of Chin et al. (1996), in which a soluble fraction is defined, limited only by the availability of H_2O_2 in the precipitating grid box. As a result, titration of SO_2 (or H_2O_2) can occur within a single time step for convection (15 min), and the associated product of oxidation subject to scavenging as sulfate aerosol. Ammonia is scavenged as a partially soluble gas determined by Henry's law. A retention efficiency of 0.05 for liquid NH_3 in cold clouds is used for 248 K < T < 268 K (mixed-phase clouds) and 0.0 for T ≤ 248 K (ice clouds). Ge et al. (2018) recently showed that the low retention of NH_3 in freezing clouds is a dominant factor responsible for the high NH_3 concentrations in the upper troposphere over the ASM region. Ammonium and nitrate are scavenged as aerosols, like sulfate.

Model results shown here are taken from parallel 6-month simulations (1 April to 1 October 2013). We describe simulations that represent (i) full chemistry, with a complete global suite of natural and anthropogenic emissions; (ii) as in (i), but with anthropogenic emissions of all species from (a) the Indian subcontinent and from (b) China eliminated.

3. Simulated Composition of ATAL

Figure 3 shows monthly mean maps of sulfate, nitrate, POA and SOA, ammonium aerosol, and ammonia gas on the 360 K surface of potential temperature, θ, for August 2013 from the standard version of the model using full chemistry (hereafter SVSim). Figure 4 shows corresponding latitude-pressure cross-sections for August, averaged between 30°E and 105°E. The 360 K surface slopes downward from ~130 hPa near the tropical tropopause to ~200 hPa in midlatitudes of the lower stratosphere, and cuts through mid-upper levels of the ATAL region (Figure 4). The ATAL is marked by an elongated region of elevated aerosols extending from North Africa to the Western North Pacific, and characterized by anticyclonic (clockwise) flow conditions, as shown by the wind vectors (red) and by closed contours of the Montgomery Stream Function (white) (Figure 3). Elevated aerosol extends across the Northern Pacific, reflecting anticyclonic eddy shedding from the ATAL region during July and August; the eastward transport extends to North America and beyond.

As shown previously by Gu et al. (2016), we find in this work that nitrate is a prominent aerosol component in the ASM anticyclone region, particularly on the southern (cold) side of the anticyclone where values above 600 ng m^{-3} (STP) are found locally (Figure 3). (We use 1,013.25 hPa and 273.15 K as STP; hereafter STP is assumed when concentrations are given). Gu et al. (2016) describe how the very low temperatures encountered in the ASM anticyclone, combined with enhanced NH_3 emissions in Asia, promote nitrate formation by shifting the gas-particle partitioning of HNO_3 toward the aerosol phase. We treat the simulated nitrate with caution in the UTLS region, however, because the ISORROPIA II model is disabled in the model stratosphere. Consequently, particulate nitrate can be advected passively where it would otherwise be expected to recycle back to HNO_3. Thus, we restrict analysis of particulate nitrate to below the tropopause and mask stratospheric levels with a small uniform positive concentration (the deep blue color in the polar regions in Figure 3b and in the stratosphere in Figures 4b and 5b).

In addition to nitrate, we find that OA and sulfate are prominent components of the simulated ATAL. Peaks of POA and sulfate aerosol are of similar magnitude in the upper troposphere in the ASM anticyclone, more than 300 ng m^{-3} (STP). We find SOA makes a larger contribution, particularly just below the tropopause (Figures 4d and 5d) with concentrations up to 50% larger than those of POA. The peak in ammonium is somewhat less than the other components. We find that BC and dust concentrations in the simulated ATAL are ~10% and ~10–20%, respectively, of POA concentrations in the upper troposphere. Specifically, maximum simulated dust concentrations were below 60 ng m^{-3} STP during August 2013 (see supporting
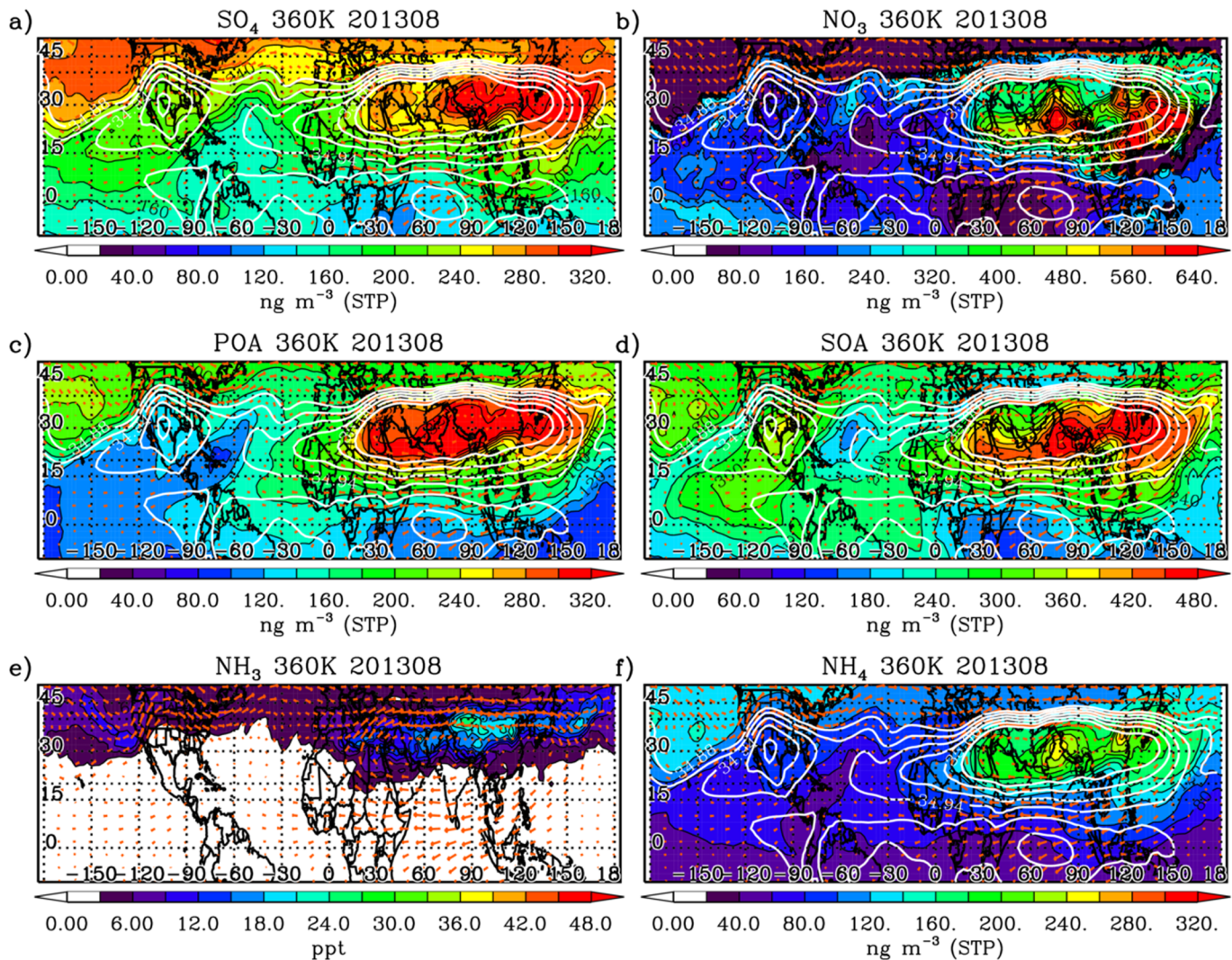
Figure 3. Maps of simulated monthly mean (a) sulfate (SO$_4$), (b) nitrate (NO$_3$), (c) primary and (d) secondary organic aerosol (POA, SOA), (e) ammonia gas (NH$_3$), and (f) ammonium (NH$_4$) aerosols at 360 K for August 2013, from the standard simulation (color-filled contours). Note scales vary for each component. Monthly mean wind vectors (red) and contours of Montgomery Stream Function (white), which lie parallel to the geostrophic flow on the potential temperature surface, are also shown. Units are ng m^{-3} STP (ng sm^{-3}) for the aerosol components, and ppt for NH$_3$. We use 273.15 K and 1,013.25 hPa as STP.

information Figure S1). Fadnavis et al. (2013) and Lau et al. (2018) show dust to be a principal component of the ATAL in their simulations. (We note that nitrate was not included in those simulations or MERRA-2 reanalyses, and that peak dust concentrations in our simulation are comparable with those shown by Fadnavis et al., ~20 ng m^{-3}). There is likely to be considerable variability between dust simulations conducted by different models due to differences in dust source distributions used; the sensitivity of dust mobilization to surface conditions, particularly surface wind (Fairlie et al., 2007); and to simulated transport from the surface to the ATAL.

Of particular interest, we find a peak in gas-phase ammonia of ~50 ppt on the northern (warm) flank of the ASM anticyclone (Figures 4e and 3e). This coincides with a minimum in nitrate (and ratio NO$_3$/(NO$_3$ + HNO$_3$); not shown) and may be due to elevated temperatures, associated with a dip in the isentropic surfaces. Höpfner et al. (2019) retrieved values of up to 150 ppt of gas-phase ammonia locally from MIPAS spectra in the upper troposphere during the ASM, and found values of up to 1 ppb in single aircraft observations obtained during StratoClim. They attributed the elevated ammonium-nitrate and gas-phase ammonia to convection of ammonia from surface sources. Simulated values do not reach those levels, due likely to the spatial and temporal averaging of both constituent distributions and convective mass fluxes. Nevertheless,
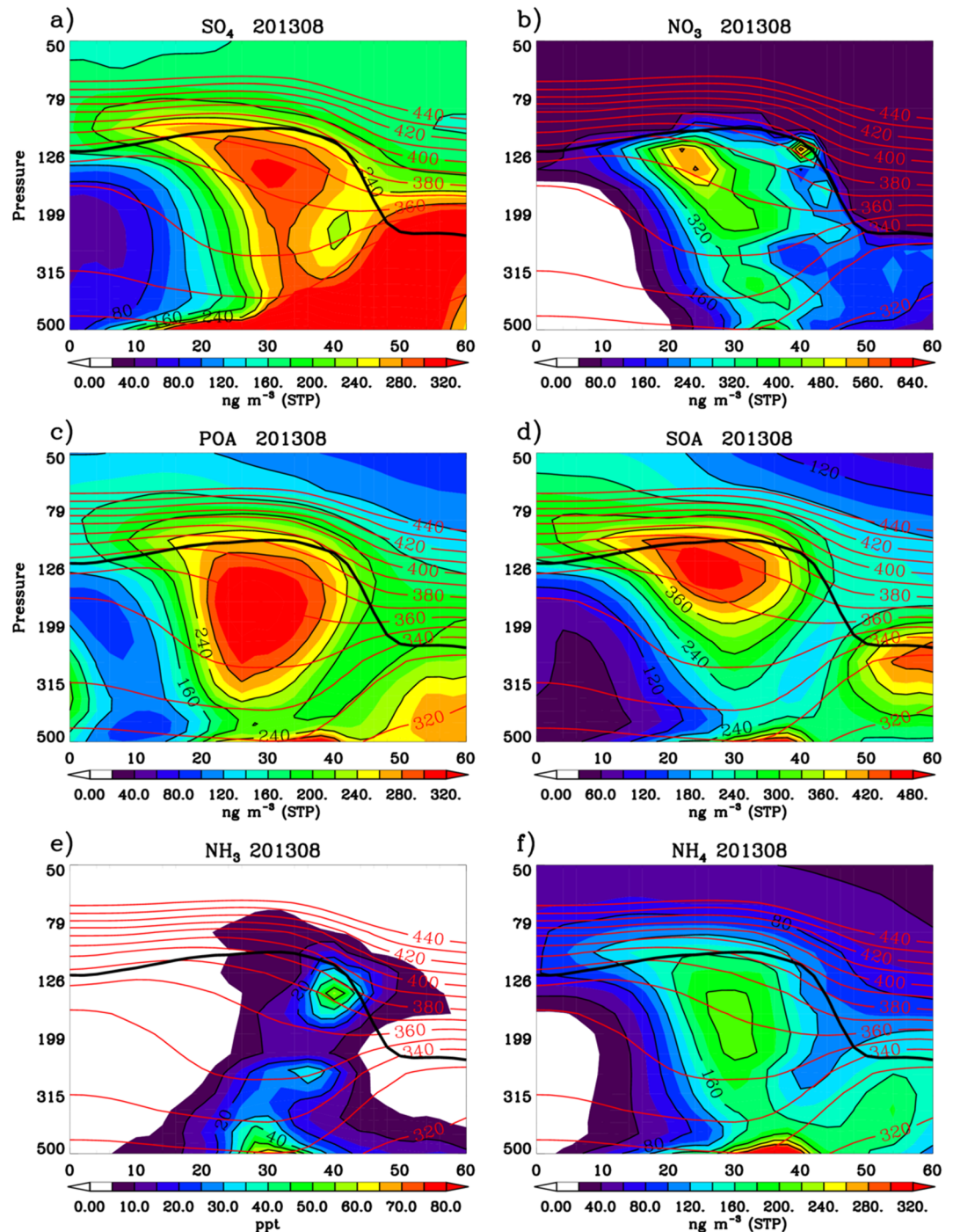
Figure 4. Latitude-pressure cross sections of simulated (a) sulfate (SO_4), (b) nitrate (NO_3), (c) primary and (d) secondary organic aerosol (POA, SOA), (e) ammonia gas (NH_3), and (f) ammonium (NH_4) aerosols for August 2013, averaged between 30°E and 105°E. Note scales vary for each component. Mean isopleths of potential temperature are also shown (red contours). Units are ng m^{-3} STP (ng sm^{-3}) for the aerosol components, and ppt for NH_3. We use 273.15 K and 1,013.25 hPa for STP. A mask of 40 ng m^{-3} is applied to NO_3 in the stratosphere (see text for details).

the model results provide evidence to support these observations of gas-phase ammonia in the vicinity of the ATAL.

Figure 5 shows corresponding longitude-pressure cross-sections averaged between 20°N and 40°N for August 2013. The vertical distributions of the aerosol components, especially sulfate and OA, reflect the
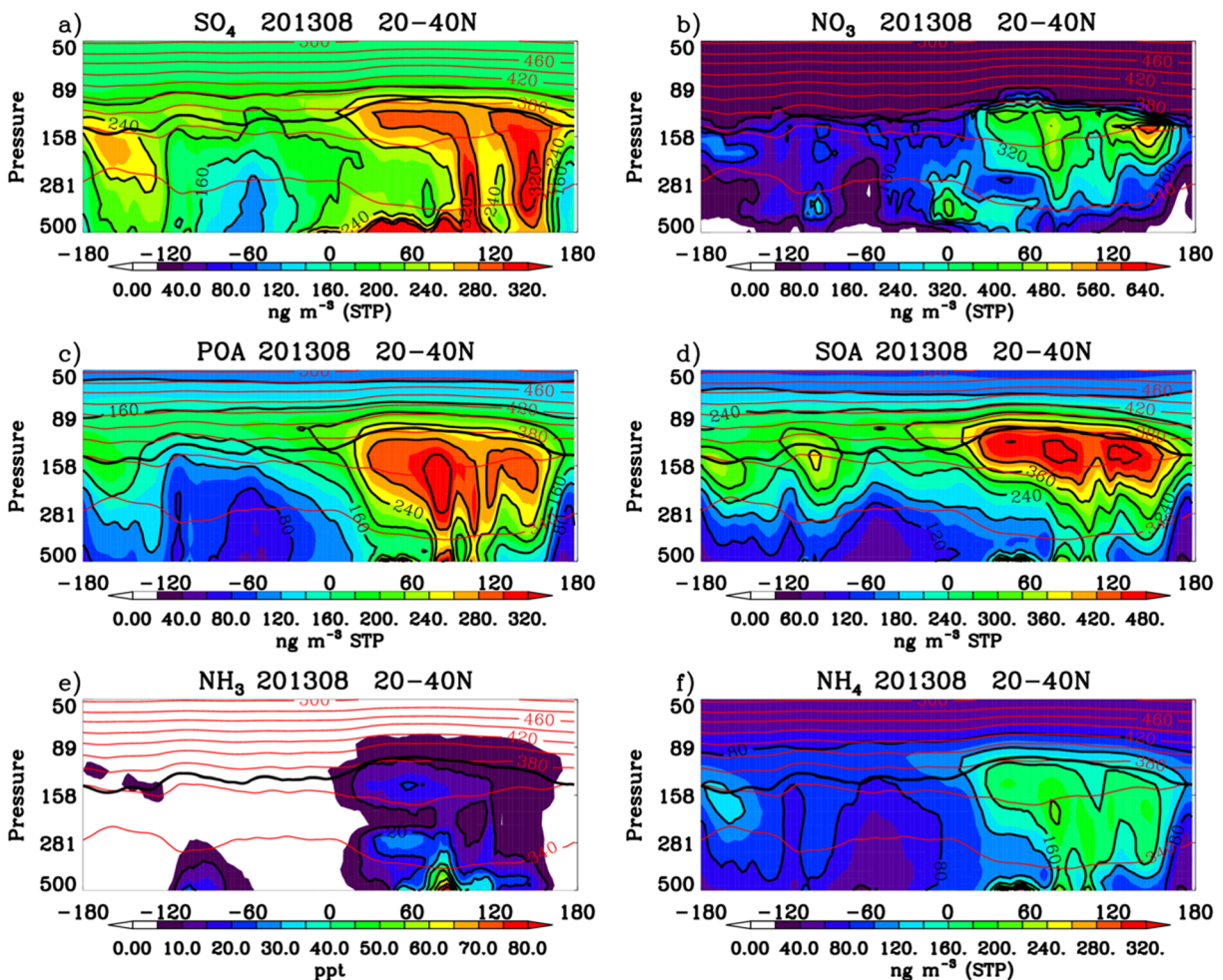
Figure 5. Longitude-pressure cross sections of simulated (a) sulfate (SO_4), (b) nitrate (NO_3), (c) primary and (d) secondary organic aerosol (POA, SOA), (e) ammonia gas (NH_3), and (f) ammonium (NH_4) aerosols for August 2013, averaged between 20°N and 40°N. Note scales vary for each component. Mean isopleths of potential temperature (K) are also shown (red contours). Mean tropopause is shown by thick black line. Units are ng m^{-3} STP for the aerosol components, and ppt for SO_2 and NH_3. We use 273.15 K and 1,013.25 hPa for STP. A mask of 40 ng m^{-3} STP is applied to NO_3 in the stratosphere (see text for details).

convective lofting and oxidation of sulfate precursor SO_2, primary organics, and secondary organic precursors to the upper troposphere especially over eastern China (100–110°E) during August 2013. The material then spreads westward as it circulates the ATAL anticyclone, but is also detrained eastward across the Pacific, illustrated by peaks in the UTLS near 180–140°W. Figure 5e also shows elevated NH_3 extending into the upper troposphere near 80°E, reflecting the strong prescribed source in northern India (Figure 2e).

Results shown in this study show some quantitative and qualitative differences from those shown by Gu et al. (2016). It is noted that Gu et al. reported aerosol concentrations (their Figure 7) in the unit of "μg m^{-3}" while we converted aerosol concentrations to standard temperature and pressure ("ng m^{-3} STP"). The aerosol distributions in the vicinity of the ATAL in our simulation exhibit more structure, which is closely aligned with the flow fields. Differences between the two studies are to be expected. Gu et al. show maps for a much earlier year, 2005, and show seasonal means (June–August), whereas we show monthly maps for 2013, for August when the ATAL is at its most intense. Seasonal averaging leads to smoother aerosol and meteorological distributions. Differences in model versions (v9-02 vs. v9-01-03) are unlikely to have impacted the inorganic aerosol results significantly, since the upgrade to v9-02 had minimal change to the treatment of inorganic aerosol. However, the treatment of SOA is improved in the model version used here, over that used by Gu et al., which severely underestimates global monoterpene emissions and does not consider isoprene SOA or anthropogenic SOA (Shah et al., 2019). The use of MERRA vs. GEOS-5 meteorological
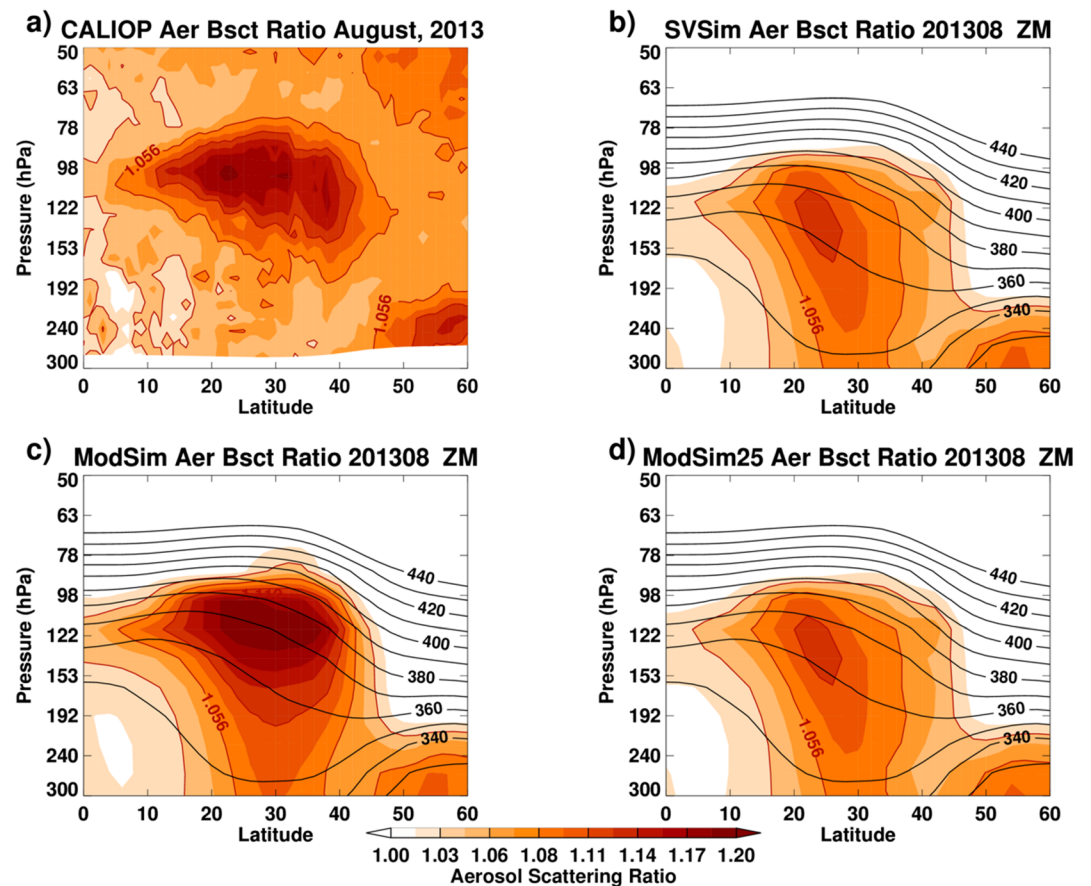
Figure 6. Latitude-pressure cross-sections of (a) CALIOP aerosol scattering ratio (SR) at 532 nm averaged over longitudes 30–105°E for August 2013 (top left); (b) corresponding SR at 550 nm diagnosed from the standard (SVSim) simulation, (c) from the simulation with modified treatment of SO_2 scavenging in convective updrafts (ModSim), and (d) same as (c) but with 25% ice retention for SO_2. Lidar ratios of 70 sr were assumed for sulfate-ammonium-nitrate, OA, and BC, and 40 sr for mineral dust to convert simulated extinction to backscatter. Contours of potential temperature (K; black) are also shown.

fields may impact aerosol transport, but the different years and seasonal vs. monthly averaging likely account for different results in the two studies.

4. Sensitivity to Wet Scavenging Efficiency of SO_2

Although the model successfully simulates an ATAL layer, we find that aerosol backscatter deduced from the simulation is biased low compared with observations. Figure 6 shows latitude-pressure cross-sections of cloud-cleared aerosol SR from CALIPSO averaged over ATAL longitudes (30–105°E) for August 2013. The ATAL is distinguished by enhanced SR between ~10°N and 45°N, 160–80 hPa (~13–17 km), reaching values of 1.1–1.2. Figure 6b shows SR from the standard (SVSim) simulation. Simulated SR values are obtained from aerosol extinction computed for each aerosol component, using prescribed optical properties and local relative humidity (Drury et al., 2010), and using lidar (extinction-to-backscatter) ratios of 70 sr for sulfate-nitrate-ammonium, organic carbon and BC aerosol and 40 sr for dust (Kim et al., 2018). The highest values of simulated SR reach only up to 1.08–1.09 in the upper troposphere, and the orientation of the observed distribution is more elongated in latitude than the simulated distribution. The standard simulation clearly underestimates aerosol backscatter in the CALIPSO observations of the ATAL. The simulated backscatter would likely be further reduced, enhancing the model bias, if particles were assumed internally mixed in the model. This is because an internal mixing assumption would decrease the aerosol number and increase mean aerosol radius compared to the external mixing assumption. Based on the aerosol optical property calculation by Curci et al. (2015), AOD with internal mixing assumption was found to be lower by
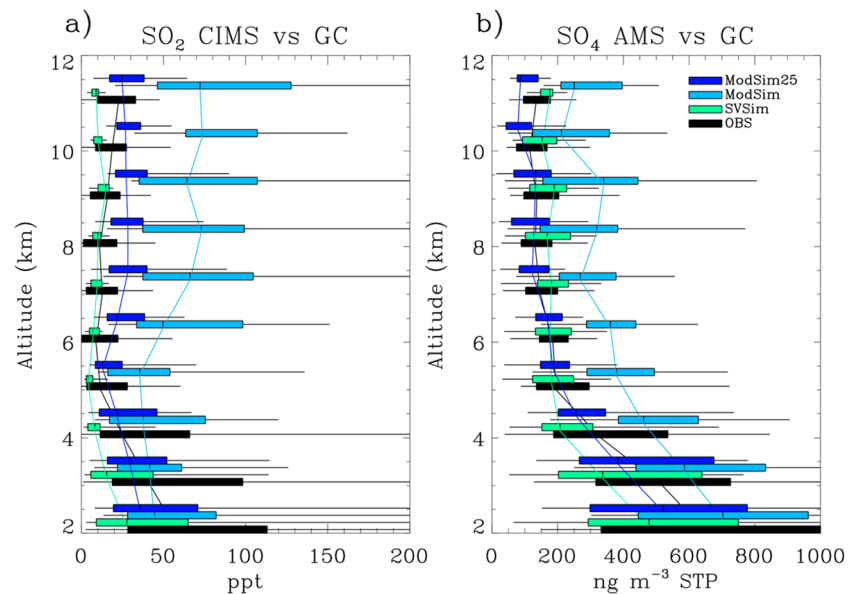
Figure 7. Vertical distribution (1 km vertical bins) of observed and simulated SO_2 and sulfate from DC8 flights made during the SEAC[4]RS airborne campaign, August–September 2013. Observations (black) are of CIMS SO_2 (a) and AMS submicron sulfate (b) obtained from 60s merge data files compiled from DC8 flights from the 6th of August to the 24th of September 2013 (data available at https://www-air.larc.nasa.gov/missions/seac4rs/index.html). The SVSim results are shown in green; results with modified treatment of SO_2 scavenging in convective updrafts (ModSim) are in pale blue; results with modified treatment of SO_2 scavenging and 25% ice retention for SO_2 in convective updrafts (ModSim25) are in dark blue. Colored bars span 25th–75th percentile; whiskers span 5th–95th percentile; colored profiles mark median values; Units are ppt (SO_2) and ng m^{-3} STP (sulfate).

~35% than AOD with external mixing assumption. Curci et al. also reported relatively small changes (~1% for homogeneous and ~11% for core-shell) of asymmetry factor with internal mixing assumptions. The model low bias may reflect underestimated surface sources, convective transport that is too weak in the model, scavenging that is too strong, or secondary aerosol production that is too weak in the upper troposphere.

We have explored whether this low bias in simulated SR in the ATAL region is associated with a deficit in simulated sulfate in the model, associated with too-rapid oxidation of SO_2 and scavenging of the resultant sulfate in convective updrafts. Simulated SO_2 in the ATAL region is below ~30 ppt over eastern China and below ~10 ppt over India and the Middle East (not shown). These values are low compared with the limited in situ observations reported from flights of high-altitude aircraft in the vicinity of the ATAL region over the last several years. SO_2 mixing ratios of 20–30 ppt have been reported between 14.5 and 15 km altitude in monsoonal outflow over the Middle East, from the High Altitude and Long Range (HALO) aircraft flown during the 2012 Earth System Model Validation (ESMVal) campaign (Roiger et al., 2013). Additionally, SO_2 mixing ratios of 50–250 ppt have been reported in the ASM anticyclone from flights of the Deutsche Forschungsanstalt für Luft- und Raumfahrt (DLR) Falcon aircraft in the 2014 Deepwave mission, and from the HALO in the 2015 OMO Asia campaign (H. Schlager, personal communication, manuscript in preparation). SO_2 mixing ratios greater than 200 ppt were reported in the upper troposphere over the Western Pacific during the PEM West A campaign, and were attributed to convective outflow of anthropogenic emissions over Asia (Thornton et al., 1997).

We evaluated the model simulated SO_2 and sulfate vertical profiles with aircraft observations from the SEAC4RS field campaign (Figure 7), which sampled convective outflow associated with the North American monsoon (Toon et al., 2016) during August–September 2013 (our simulation year). SO_2 measurements shown in Figure 7 were made with the Georgia Institute of Technology chemical ionization mass spectrometer (CIMS) (Huey, 2007); submicron sulfate measurements were made using the University of Colorado, Boulder, Aerosol Mass Spectrometer (AMS) (Dunlea et al., 2009). Kim et al. (2015) conducted a high-resolution, nested-grid simulation of the southeast United States during SEAC4RS using GEOS-Chem; they included an additional mechanism for SO_2 oxidation in the model (Criegee biradical

mechanism) to counter a low sulfate bias; they show median simulated sulfate ~20% low below 4 km altitude, but in good agreement with observations above (their Figure S4). However, they show simulated SO_2 extremely low with respect to observations above 2 km altitude. Results from our simulation show simulated SO_2 (green) 40–60% low compared with the CIMS observations (black) above ~9 km altitude and 50–70% low below ~6 km, while simulated sulfate shows a 30–40% positive bias in the upper troposphere and a 25–35% negative bias in the lower troposphere.

In the standard GEOS-Chem, the fraction of SO_2 available for scavenging in convective updrafts is limited only by the availability of H_2O_2 in the precipitating grid box (section 2.2), with the oxidation product scavenged as sulfate aerosol. This treatment results in very efficient removal of SO_2 in wet convective updrafts in the ASM, and only a moderate enhancement of sulfate aerosol in the ASM anticyclone (Figures 3–5). Since SO_2 is only partially soluble, and the time scale for in-cloud oxidation by H_2O_2 is similar to that for convection, titration of the limiting reagent (SO_2 or H_2O_2) within a single 15-min time step may substantially overestimate the rate of SO_2 oxidation and subsequent loss from wet scavenging.

To address this issue, we combined an effective Henry's law formulation for the dissolution of SO_2 with a kinetic solution to in-cloud oxidation to compute the fraction of SO_2 available for wet scavenging in convective updrafts. The same approach is used elsewhere in the model for in-cloud sulfate production. The resultant rate of loss of SO_2 from H_2O_2 oxidation, L (v/v/time step), is expressed as

$$L = [SO_2][H_2O_2](\exp(X)-1)/([SO_2]\exp(X)-[H_2O_2]),$$

following Laidler (1987) (p.24–25), where the exponent X is given by

$$X = ([SO_2]-[H_2O_2]) \, K_{aq}H_2O_2 \, \frac{\Delta z}{V_{ud}},$$

where rate constant $K_{aq}H_2O_2$ is the rate of aqueous phase oxidation of S (IV) by H_2O_2, $[SO_2]$, and $[H_2O_2]$ are the respective volume mixing ratios, and $\Delta t = \Delta z/V_{ud}$ is a measure of the in-cloud residence time for an air parcel with updraft velocity V_{ud} (m s^{-1}) in a model grid box of thickness Δz (section 2.2). An analogous formulation is used for the loss rate of SO_2 due to in-cloud oxidation by ozone. Calculation of the effective Henry's constant, and rate constants $K_{aq}H_2O_2$, and $K_{aq}O_3$ (for ozone), follows Seinfeld and Pandis (1998) (p.350–351, p.363–366) with equilibrium reaction constants taken from Jacob (1986). Cloud water pH is obtained in the model by assuming electro-neutrality (Alexander et al., 2012).

This approach moderates the scavenging of SO_2, permitting more to be lofted to the upper troposphere, and results in more sulfate aloft. Figure 6c shows that the resultant backscatter ratios (ModSim simulation) more closely match those obtained from cloud-cleared CALIPSO observations (Figure 6a), and shows a distribution which better matches the shape and pressure range where CALIPSO observes the ATAL. Despite this, we find that in the SEAC4RS domain, the model produces SO_2 and sulfate enhancements that are too high in the upper troposphere compared to those observed (Figure 7, pale blue bars). By retaining 25% of SO_2 in cold cloud (<248 K) in the model, which is subject to scavenging by ice, we can reduce simulated SO_2 and sulfate to levels more consistent with the SEAC4RS observations (Figure 7, dark blue bars, labelled ModSim25), but at a cost of reducing SR values (Figure 6d) to levels of those from the standard (SVSim) simulation. In their modeling studies of convective outflow, Bela et al. (2016) required complete retention of SO_2 on freezing of cloud water to reproduce observations in convective outflow made during the Deep Convective Clouds and Chemistry (DC3) field campaign. Our experiments indicate that reducing the efficiency of scavenging of SO_2 in convective updrafts in order to enhance sulfate aloft does alleviate the low bias in SR in the ATAL region, shown in the SVSim simulation, but does not provide a global solution that works globally.

The most likely explanation for this deficiency is that convective transport in the model, especially in the ATAL region, is too weak. Yu et al. (2018) demonstrated that remapping of meteorological data from the native cubed-sphere grid of the parent GCM (GEOS-5) to an equivalent-resolution latitude-longitude grid, and 3-hr-averaging of the fields, led to vertical transport errors of 20% in offline CTM (GEOS-Chem) simulations of a surface-source tracer, ^{222}Rn, compared to online ^{222}Rn simulations (their Figure 2). Yu et al. (2018) attributed this error, in part, to a loss of transient organized vertical motions. Further degradation of the spatial resolution of the meteorological data to 2° × 2.5° (as used in our study) led to ^{222}Rn concentrations biased

40% low in the upper troposphere, relative to online ^{222}Rn simulations (their Figure 3), due to further weakening of vertical transport via spatial averaging.

Excessive scavenging of other aerosol components, e.g., POA and SOA precursors, or SOA production in the ATAL that is too weak, may also contribute to the deficit. However, Pai et al. (2019) indicate that GEOS-Chem does not generally underestimate OA in the upper troposphere, although their comparisons with data are limited to below 10 km. The study by Yu et al. (2018) indicates that intensification of simulated convection in the Asian monsoon region would raise aerosol concentrations (and SR values) in the simulated ATAL, similar to that achieved in limiting SO$_2$ scavenging (ModSim). Assuming lower lidar ratios to convert modeled extinction coefficient to SR does not solve the problem; the peak in simulated SR is intensified, but the vertical distribution (i.e., the shape) remains unaffected.

5. Contribution of Anthropogenic Regional Sources to ATAL Composition

We revert to the standard simulation (SVSim) to estimate the contribution of regional anthropogenic vs. external sources to the ATAL. We conducted parallel simulations using GEOS-Chem in which we eliminated anthropogenic emissions over the Indian subcontinent and over China (see, e.g., maps of SO$_2$ emissions in Figures 2c and 2f). (Here anthropogenic emissions are specified as fossil fuel plus biofuel emissions). The regional contributions are then estimated as differences between the simulations that include all sources and those with regional anthropogenic sources eliminated. Residual differences between the simulations with all sources and with summed contributions from the regional anthropogenic sources are interpreted as accounting for natural and extraregional contributions. This assumes that contributions sum linearly, which is not always the case, because of nonlinear dependencies between aerosol components.

Figures 8 and 9 show the percent contributions from the Indian subcontinent (top rows), and from Chinese (middle rows) anthropogenic emissions on sulfate, nitrate, ammonium, and POA and SOA concentrations in the ATAL at 360 K for August 2013 from the model. We first discuss sulfate and OA simulations, followed by nitrate and ammonium. The North Indian source region lies directly beneath the ASM anticyclone for much of summer in 2013, and vertical transport of North Indian sources provides a compact contribution of up to 40% (sulfate), up to 65% (POA), and up to 40% (SOA) confined by the ATAL anticyclone at this time. The East China source region lies mostly east of the core of anticyclonic flow during the 2013 ASM, but makes a contribution reaching 60% (both sulfate and POA) and 30% (SOA) in the eastern part of the ATAL region and up to 40% (sulfate and POA) and 20% (SOA) in a horseshoe around the southern flank of the anticyclone, reflecting horizontal transport by strong winds following convective lofting of surface emissions (Liu et al., 2002). Chinese sources also make a significant contribution (30–35%) to transport of sulfate and POA across the northern Pacific, and across the tropical Atlantic (30–40%) in the UT. Also shown in Figures 8 and 9 (bottom rows) are residual contributions at the same level for the same month, which we attribute to nonanthropogenic (i.e., not fossil-fuel or biofuel) sources and sources external to China and the Indian subcontinent. We find minima of ~20% contribution to sulfate (~10% for POA and ~50% for SOA) in the ATAL region from these sources, reflecting in part the effective transport barrier associated with the ASM anticyclone (Ploeger et al., 2015), and in the case of SOA the dominance of biogenic over anthropogenic sources (Heald et al., 2011). In the case of sulfate, these results contrast with those of Neely et al. (2014), who determined that regional sources contributed only ~30% to sulfate in the ATAL region. It is possible that weaker convective transport, lack of in-cloud production of sulfate, or more efficient scavenging of pollution in the ATAL region resulted in a larger relative contribution from sources external to the region in their study.

The percent contributions to ammonium aerosol are distributed similarly to that for OAs (Figures 8c, 8f, 8i, and 9) in the ATAL region, with up to 65% from sources of the Indian subcontinent, and a residual contribution ~10%. This likely reflects high ammonia emissions over North India (Figure 2e). Contributions to ammonium from Chinese emissions peak in the eastern part of the ATAL anticyclone and show the characteristic horseshoe around the eastern and southern flanks of the anticyclone. For nitrate, we again focus on distributions below the tropopause, for the reasons given earlier. In the ATAL region, contributions from Indian regional anthropogenic sources reach peaks of up to 80% in the western core of the ATAL region, while Chinese contributions peak on the southern and eastern flanks of the anticyclone where nitrate
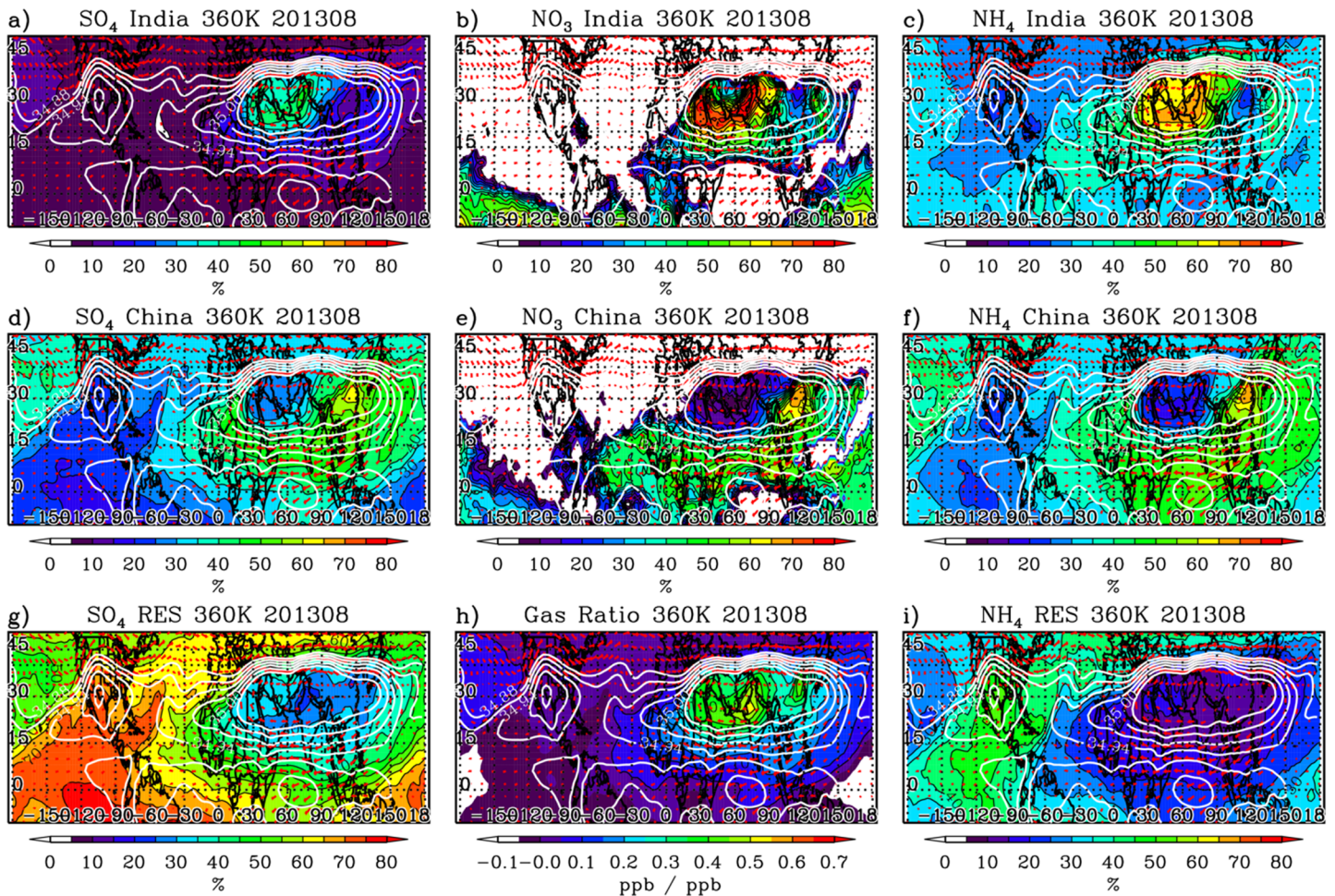
Figure 8. Simulated percent contributions of sulfate, nitrate, and ammonium aerosols from anthropogenic Indian (panels a–c), Chinese (panels d–f) sources at 360 K for August 2013 (color-filled contours). Units are %. The residual (rest-of-the-world) sulfate and ammonium contributions are shown (panels g and i); Gas ratio (see text for details) is also shown (panel h; units: ppb/ppb). Also shown are wind vectors (red) and contours of Montgomery Stream function (white contours). Contributions of nitrate are shown only where the 360 K surface lies below the tropopause.

concentrations are highest (Figures 3 and 4). Farther afield, over North America, e.g., we find that eliminating Chinese or Indian anthropogenic emissions actually *increase* nitrate (negative residual percent values, which are not shown), albeit in regions where nitrate is generally small (Figure 3). This is consistent with nonlinearity in the sulfate-nitrate-ammonium system (Ansari & Pandis, 1998); while anthropogenic emissions (NO_x, NH_3, SO_2) from India lead to enhancements of nitrate in the near field, e.g., displacement of nitrate by the resultant sulfate contribution can lead to reductions in nitrate elsewhere. Figure 8h shows the gas ratio, GR, defined as the free ammonia, divided by total nitrate: $GR = ([NH_3] + [NH_4^+] - 2[SO_4^=]) / ([NO_3^-] + [HNO_3^-])$ (Ansari & Pandis, 1998). While we find ammonia in excess (GR > 5) at low altitudes above South Asia, the August mean at 360 K shows GR very low (<~0.4) for which such nonlinear behavior is expected.

Interannual and intraseasonal variability is expected in the relative contributions to the ATAL from the different anthropogenic source regions, because of variability in the spatial extent and morphology of the ASM anticyclone. Specifically, source regions can directly impact the ATAL via convection when the core or a lobe of the anticyclone lies directly above the source. As Indian sources of SO_2 continue to grow while China sources diminish (Li et al., 2017), for those years in which Indian sources dominate, the ATAL sulfate may become more prevalent in the ATAL compared with nitrate.
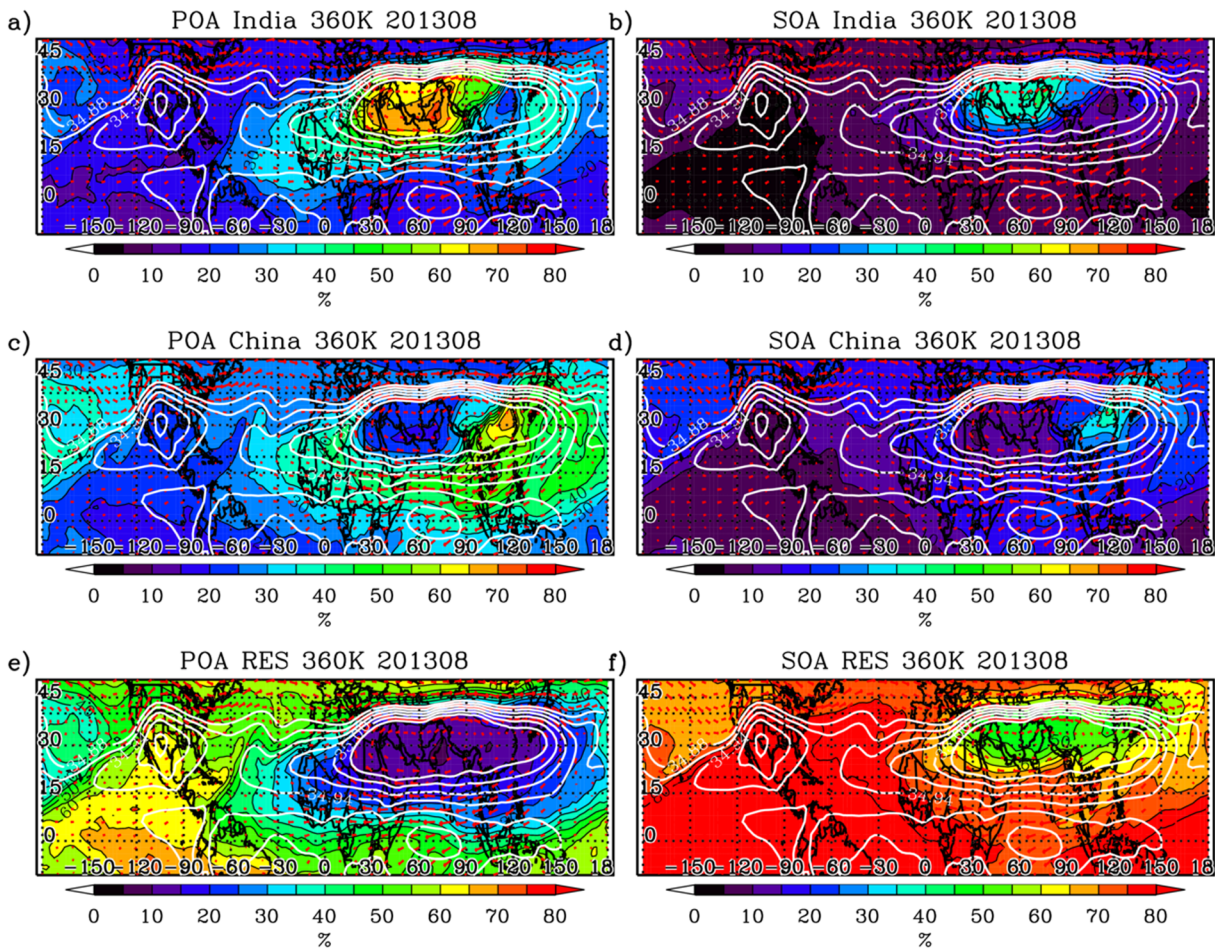
Figure 9. Same as Figure 8, but for simulated percent contributions of primary organic aerosol (POA) and secondary organic aerosol (SOA) from anthropogenic Indian (a–b), Chinese (c–d), and residual (rest-of-the-world) (e–f) sources at 360 K for August 2013. Units are %. Also shown are contours of Montgomery Stream function (white).

6. Contribution of Lightning NO$_x$ to Nitrate in the ATAL

The ASM is associated not only with deep convection but also with significant lightning discharge. Using the GEOS-Chem model, Barret et al. (2016) previously showed that Asian lightning NO$_x$ emissions make a major contribution to the photochemical ozone production within the ASM anticyclone. On the other hand, the direct impact of lightning NO$_x$ emissions on chemical and microphysical properties of global UT aerosols has recently received attention (Tost, 2017). Tost showed a major contribution from lightning NO$_x$ emissions to the UT nitrate aerosol burden in a global chemistry-climate model. In this study, we conducted an additional simulation to assess the importance of lightning sources of NO$_x$ to nitrate concentrations in the ATAL. Figure 10 shows zonal cross-sections of nitrate from (a) the SVSim (also shown in Figure 4b), (b) the simulation with lightning NO$_x$ sources removed, and (c) the difference. A fourth cross-section (d) shows nitrate from the simulation with global anthropogenic sources removed. The figure shows that removing lightning NO$_x$ sources results in a 10–15% reduction in nitrate where nitrate peaks in the upper troposphere on the southern flank of the ASM anticyclone. At lower altitudes between 30°N and 50°N, the percent reduction is somewhat larger (~20%). With global anthropogenic emissions eliminated, nitrate concentrations are much reduced in the upper troposphere in the vicinity of the ASM with a peak of only ~200 ng m^{-3} on the northern side of the ASM anticyclone. The figure reemphasizes that anthropogenic emissions dominate the nitrate concentration in the ATAL, with lightning sources of NO$_x$ contributing about 10–15%. The origin of differences between the distributions shown in panels (c) and (d) is unclear, but is likely associated with contributions from other natural sources (e.g., soil, agriculture, and fires) of nitrate precursors. The feature
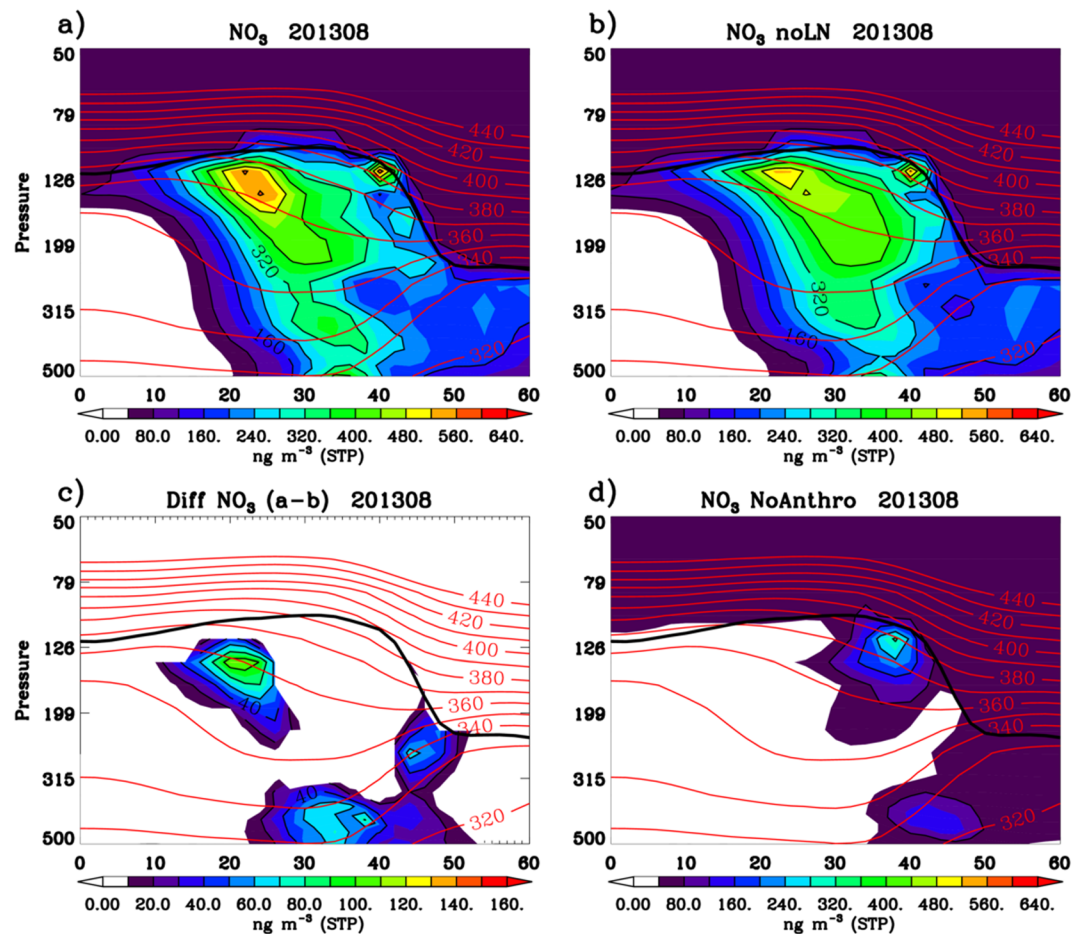
Figure 10. Latitude-pressure cross sections of simulated nitrate aerosol for August 2013, averaged between 30°E and 105°E (panel a); (b) as in (a) but without lightning NO_x sources; (c) difference of (a) and (b); (d) as in (a) but without global anthropogenic emissions. Mean isopleths of potential temperature (K) are also shown (red contours). Units are ng m^{-3} STP. A mask of 40 ng m^{-3} STP is applied to NO_3 in the stratosphere (see text for details).

near the tropopause at ~38°N, 130 hPa (peak value) in panels a, b, and d is regarded as an artifact resulting from unrealistic stratospheric values (section 3).

7. Summary and Conclusions

We have used the GEOS-Chem CTM to simulate the composition of the ATAL for summer 2013, and to estimate regional contributions from anthropogenic source regions in the Indian subcontinent and China. The model shows significant sulfate, ammonium, and OA with a prominent nitrate contribution, as identified by Gu et al. (2016) using an earlier version of the model, and SOA concentrations that exceed those due to primary sources. In a new finding, the model indicates the presence of gas-phase ammonia, preferentially on the northern flank of the ASM anticyclone. This provides evidence to support spectral measurements made from the MIPAS satellite and aircraft limb IR measurements during the StratoClim campaign (Höpfner et al., 2016, 2019). Backscatter estimates diagnosed from the model simulation are low compared with those obtained from CALIPSO observations. We explored whether this deficit could be explained by too-rapid oxidation of SO_2 and scavenging of resultant sulfate in convective precipitation in the model. A low bias of SO_2 is characteristic of the model in the upper troposphere, as evidenced in part by comparison with SEAC4RS aircraft observations. We found that the application of a Henry's law formulation for the dissolution of SO_2 and a kinetic solution to in-cloud oxidation corrected the deficit in simulated backscatter by increasing sulfate in the ATAL region, but introduced an unacceptably high bias in SO_2 and sulfate compared with

SEAC4RS data. With 25% of SO_2 retained in cold clouds (<248 K) in the model, the simulated SO_2 and sulfate levels would be more consistent with the SEAC4RS observations, but at a cost of reducing aerosol backscatter. Sulfate thus may not be the main contributor to the deficit in backscatter. Recent balloon-based in situ observations of ATAL composition (Vernier et al., 2018) and data from the StratoClim airborne campaign (Höpfner et al., 2019) also suggest that sulfate may not be as important a component of the ATAL as previously assumed. The most likely explanation for this deficiency is that convective transport in the model, especially in the ATAL region, is too weak. Underestimated SOA production in the ATAL, or excessive scavenging of other aerosol components and precursors in the model may also contribute to the deficit and can be explored in future studies.

We conducted source apportionment simulations in which anthropogenic (fossil fuel and biofuel) emissions were eliminated in the source regions of the Indian subcontinent and China. For the case of August 2013, we found that Indian sources contribute up to 40% of sulfate and up to 65% of organic and ammonium aerosol in the western ATAL region. Chinese sources contributed up to 60% in the eastern ATAL, up to 40% (sulfate, organic, and ammonium aerosol) in a horseshoe on the southern flank of the ASM anticyclone region, and to transport across the Pacific in the upper troposphere. Nitrate aerosol is found to be a dominant component of aerosol composition on the southern flank of the ASM anticyclone. Nitrate does not respond linearly to elimination of regional anthropogenic sources, likely due to competition for ammonium from sulfate. Lightning sources of NO_x are found to make a significant (10–15%) contribution to nitrate in the ATAL for the case studied. Convective sources over China are located primarily on the flank of the ASM anticyclone for this case, and less constrained by the circulation. The dominance of regional sources found here contrasts with results obtained by Neely et al. (2014) who found that regional sources contributed only ~30% to sulfate in the ATAL. It should be noted that considerable interannual and intraseasonal variability exists in the morphology and spatial extent of the ASM anticyclone. The patterns and relative contributions from these regional source regions are expected to differ significantly from year to year from those shown here, and will be explored in future work.

References

Alexander, B., Allman, D. J., Amos, H. M., Fairlie, T. D., Dachs, J., Hegg, D. A., & Sletten, R. S. (2012). Isotopic constraints on sulfate aerosol formation pathways in the marine boundary layer of the subtropical northeast Atlantic Ocean. *Journal of Geophysical Research*, *117*, D06304. https://doi.org/10.1029/2011JD016773

Alexander, B., Park, R. J., Jacob, D. J., & Gong, S. (2009). Transition metal-catalyzed oxidation of atmospheric sulfur: Global implications for the sulfur budget. *Journal of Geophysical Research*, *114*, D02309. https://doi.org/10.1029/2008JD010486

Ansari, A. S., & Pandis, S. N. (1998). Response of inorganic PM to precursor concentrations. *Environmental Science & Technology*, *32*, 2706–2714.

Barret, B., Sauvage, B., Bennouna, Y., & Le Flochmoen, E. (2016). Upper-tropospheric CO and O_3 budget during the Asian summer monsoon. *Atmospheric Chemistry and Physics*, *16*, 9129–9147. https://doi.org/10.5194/acp-16-9129-2016

Bela, M. M., Barth, M. C., Toon, O. B., Fried, A., Homeyer, C. R., Morrison, H., et al. (2016). Wet scavenging of soluble gases in DC3 deep convective storms using WRF-Chem simulations and aircraft observations. *Journal of Geophysical Research: Atmospheres*, *121*, 4233–4257. https://doi.org/10.1002/2015JD024623

Bergman, J. W., Fierli, F., Jensen, E. J., Honomich, S., & Pan, L. L. (2013). Boundary layer sources for the Asian anticyclone: Regional contributions to a vertical conduit. *Journal of Geophysical Research: Atmospheres*, *118*, 2560–2575. https://doi.org/10.1002/jgrd.50142

Bond, T. C., Bhardwaj, E., Dong, R., Jogani, R., Jung, S., Roden, C., et al. (2007). Historical emissions of black and organic carbon aerosol from energy-related combustion, 1850-2000. *Global Biogeochemical Cycles*, *21*, GB2018. https://doi.org/10.1029/2006GB002840

Chin, M., Jacob, D. J., Gardner, G. M., Foreman-Fowler, M. S., & Spiro, P. A. (1996). A global three-dimensional model of tropospheric sulfate. *Journal of Geophysical Research*, *101*(D13), 18,607–18,690.

Cooke, W. F., Liousse, C., Cachier, H., & Feichter, , J. (1999). Construction of a 1° x 1° fossil fuel emission data set for carbonaceous aerosol and implementation and radiative impact in the ECHAM-4 model. *Journal of Geophysical Research*, *104*, 22,137–22,162

Curci, G., Hogrefe, C., Bianconi, R., Im, U., Balzarini, A., Baró, R., et al. (2015). Uncertainties of simulated aerosol optical properties induced by assumptions on aerosol physical and chemical properties: An AQMEII-2 perspective. *Atmospheric Environment*, *115*, 541–552. https://doi.org/10.1016/j.atmosenv.2014.09.009

Drury, E., Jacob, D. J., Spurr, R. J. D., Wang, J., Shinozuka, Y., Anderson, B. E., et al. (2010). Synthesis of satellite (MODIS), aircraft (ICARTT), and surface (IMPROVE, EPA-AQS, AERONET) aerosol observations over eastern North America to improve MODIS aerosol retrievals and constrain surface aerosol concentrations and sources. *Journal of Geophysical Research*, *115*, D14204. https://doi.org/10.1029/2009JD012629

Duncan, B. N., Martin, R. V., Staudt, A. C., Yevich, R., & Logan, J. A. (2003). Interannual and seasonal variability of biomass burning emissions constrained by satellite observations. *Journal of Geophysical Research*, *108*(D2), 4100. https://doi.org/10.1029/2002JD002378

Dunlea, E. J., DeCarlo, P. F., Aiken, A. C., Kimmel, J. R., Peltier, R. E., Weber, R. J., et al. (2009). Evolution of Asian aerosols during transpacific transport in INTEX-B. *Atmospheric Chemistry and Physics*, *9*, 7257–7287.

Fadnavis, S., Kalita, G., Kumar, K. R., Gasparini, B., & Li, J.-L. F. (2017). Potential impact of carbonaceous aerosol on the upper troposphere and lower stratosphere (UTLS) and precipitation during Asian summer monsoon in a global model simulation. *Atmospheric Chemistry and Physics*, *17*, 11,637–11,654. https://doi.org/10.5194/acp-17-11637-2017

Fadnavis, S., Semeniuk, K., Pozzoli, L., Schultz, M. G., Ghude, S. D., Das, S., & Kakatkar, R. (2013). Transport of aerosols into the UTLS and their impact on the Asian monsoon region as seen in a global model simulation. *Atmospheric Chemistry and Physics*, *13*, 8771–8786.

Fairlie, T. D., Liu, H., Vernier, J.-P., Campuzano-Jost, P., Jimenez, J. L., Jo, D., et al. (2019). GEOS-Chem v9-02 with simple SOA scheme for ATAL simulations & model output [Data set]. *Zenodo*. http://doi.org/10.5281/zenodo.3596152

Fairlie, T. D., Jacob, D. J., & Park, R. J. (2007). The impact of transpacific transport of mineral dust in the United States. *Atmospheric Environment*, *41*(6), 1251–1266.

Fairlie, T. D., Vernier, J.-P., Natarajan, M., & Bedka, K. M. (2014). Dispersion of the Nabro volcanic plume and its relation to the Asian summer monsoon. *Atmospheric Chemistry and Physics*, *14*, 7045–7057. https://doi.org/10.5194/acp-14-7045-2014

Farmer, D. K., Matsunaga, A., Docherty, K. S., Surratt, J. D., Seinfeld, J. H., Ziemann, P. J., & Jimenez, J. L. (2010). Response of an aerosol mass spectrometer to organonitrates and organosulfates and implications for atmospheric chemistry. *Proceedings of the National Academy of Sciences of the USA*, *107*, 6670–6675. https://doi.org/10.1073/pnas.0912340107

Fountoukis, C. & Nenes, A. (2007). ISORROPIA II: a computationally efficient thermodynamic equilibrium model for $K^+–Ca^{2+}–Mg^{2+}–NH_4^+–Na^+–SO_4^{2−}–NO_3^−–Cl^−–H_2O$ aerosols. *Atmospheric Chemistry and Physics*, *7*, 4639–4659. https://doi.org/10.5194/acp-7-4639-2007

Garny, H., & Randel, W. J. (2016). Transport pathways from the Asian monsoon anticyclone to the stratosphere. *Atmospheric Chemistry and Physics*, *16*, 2703–2718. https://doi.org/10.5194/acp-16-2703-2016

Ge, C., Zhu, C., Francisco, J. S., Zeng, X. C., & Wang, J. (2018). A molecular perspective for global modeling of upper atmospheric NH_3 from freezing clouds. *Proceedings of the National Academy of Sciences*, *115*(24), 6147–6152. https://doi.org/10.1073/pnas.1719949115

Gu, Y., Liao, H., & Bian, J. (2016). Summertime nitrate aerosol in the upper troposphere and lower stratosphere over the Tibetan Plateau and the South Asian summer monsoon region. *Atmospheric Chemistry and Physics*, *16*, 6641–6663. https://doi.org/10.5194/acp-16-6641-2016

Guenther, A. B., Jiang, X., Heald, C. L., Sakulyanontvittaya, T., Duhl, T., Emmons, L. K., & Wang, X. (2012). The Model of Emissions of Gases and Aerosols from Nature version 2.1 (MEGAN2.1): An extended and updated framework for modeling biogenic emissions. *Geoscientific Model Development*, *5*, 1471–1492. https://doi.org/10.5194/gmd-5-1471-2012

Heald, C. L., Coe, H., Jimenez, J. L., Weber, R. J., Bahreini, R., Middlebrook, A. M., et al. (2011). Exploring the vertical profile of atmospheric organic aerosol: Comparing 17 aircraft field campaigns with a global model. *Atmospheric Chemistry and Physics*, *11*, 12,673–12,696. https://doi.org/10.5194/acp-11-12673-2011

Hodzic, A., Campuzano-Jost, P., Bian, H., Chin, M., Colarco, P. R., Day, D. A., et al. (2019). Characterization of organic aerosol across the global remote troposphere: A comparison of ATom measurements and global chemistry models. *Atmospheric Chemistry and Physics Discussions*. https://doi.org/10.5194/acp-2019-773

Hodzic, A., & Jimenez, J. L. (2011). Modeling anthropogenically controlled secondary organic aerosols in a megacity: A simplified framework for global and climate models. *Geoscientific Model Development*, *4*, 901–917. https://doi.org/10.5194/gmd-4-901-2011

Höpfner, M., Ungermann, J., Borrmann, S., Wagner, R., Spang, R., Riese, M., et al. (2019). Ammonium nitrate particles formed in upper troposphere from ground ammonia sources during Asian monsoons. *Nature Geoscience*, *12*(8), 608–612. https://doi.org/10.1038/s41561-019-0385-8

Höpfner, M., Volkamer, R., Grabowski, U., Grutter, M., Orphal, J., Stiller, G., et al. (2016). First detection of ammonia (NH_3) in the Asian summer monsoon upper troposphere. *Atmospheric Chemistry and Physics*, *16*, 14357–14369. https://doi.org/10.5194/acp-16-14357-2016

Huey, L. G. (2007). Measurement of trace atmospheric species by chemical ionization mass spectrometry: Speciation of reactive nitrogen and future directions. *Mass Spectrometry Reviews*, *26*(2), 166–184.

Jacob, D. J. (1986). Chemistry of OH in remote clouds and its role in the production of formic acid and peroxymonosulfate. *Journal of Geophysical Research*, *91*(D9), 9807–9826.

Jaeglé, L., Quinn, P. K., Bates, T. S., Alexander, B., & Lin, J.-T. (2011). Global distribution of sea salt aerosols: new constraints from in situ and remote sensing observations. *Atmospheric Chemistry and Physics*, *11*, 3137–3157. https://doi.org/10.5194/acp-11-3137-2011

Kim, M.-H., Omar, A. H., Tackett, J. L., Vaughan, M. A., Winker, D. M., Trepte, C. R., et al. (2018). The CALIPSO version 4 automated aerosol classification and lidar ratio selection algorithm. *Atmospheric Measurement Techniques*, *11*(11), 6107–6135. https://doi.org/10.5194/amt-11-6107-2018

Kim, P. S., Jacob, D. J., Fisher, J. A., Travis, K., Yu, K., Zhu, L., et al. (2015). Sources, seasonality, and trends of southeast US aerosol: An integrated analysis of surface, aircraft, and satellite observations with the GEOS-Chem chemical transport model. *Atmospheric Chemistry and Physics*, *15*(18), 10,411–10,433. https://doi.org/10.5194/acp-15-10411-2015

Laidler, K. J. (1987). *Chemical kinetics* (3rd ed.p. 544). Chennai, India: Pearson Education. ISBN: 8131709728.

Lau, W., Yuan, C., & Li, Z. (2018). Origin, maintenance and variability of the Asian Tropopause Aerosol Layer (ATAL): The roles of monsoon dynamics. *Scientific Reports*, *8*(1), 1–14.

Li, C., McLinden, C., Fioletov, V., Krotkov, N., Carn, S., Joiner, J., et al. (2017). India is overtaking China as the World's largest emitter of anthropogenic sulfur dioxide. *Scientific Reports*, *7*, 14304.

Li, Q., Jiang, J. H., Wu, D. L., Read, W. G., Livesey, N. J., Waters, J. W., et al. (2005). Convective outflow of South Asian pollution: A global CTM simulation compared with EOS MLS observations. *Geophysical Research Letters*, *32*, L14826. https://doi.org/10.1029/2005GL022762

Liu, H., Jacob, D. J., Bey, I., & Yantosca, R. M. (2001). Constraints from ^{210}Pb and ^7Be on wet deposition and transport in a global three-dimensional chemical tracer model driven by assimilated meteorological fields. *Journal of Geophysical Research*, *106*(D11), 12,109–12,128.

Liu, H., Jacob, D. J., Chan, L. Y., Oltmans, S. J., Bey, I., Yantosca, R. M., et al. (2002). Sources of tropospheric ozone along the Asian Pacific Rim: An analysis of ozonesonde observations. *Journal of Geophysical Research*, *107*(D21), 4573. https://doi.org/10.1029/2001JD002005

Mari, C., Jacob, D. J., & Bechtold, P. (2000). Transport and scavenging of soluble gases in a deep convective cloud. *Journal of Geophysical Research*, *105*(D17), 22,255–22,267.

Martinsson, B. G., Friberg, J., Andersson, S. M., Weigelt, A., Hermann, M., Assmann, D., et al. (2014). Comparison between CARIBIC aerosol samples analysed by accelerator-based methods and optical particle counter measurements. *Atmospheric Measurement Techniques*, *7*, 2581–2596. https://doi.org/10.5194/amt-7-2581-2014

Molod, A., Takacs, L., Suarez, M., & Bacmeister, J. (2015). Development of the GEOS-5 atmospheric general circulation model: evolution from MERRA to MERRA2. *Geoscientific Model Development*, *8*, 1339–1356. https://doi.org/10.5194/gmd-8-1339-2015

Neely, R. R. III, Yu, P., Rosenlof, K. H., Toon, O. B., Daniel, J. S., Solomon, S., & Miller, H. L. (2014). The contribution of anthropogenic SO_2 emissions to the Asian tropopause aerosol layer. *Journal of Geophysical Research: Atmospheres*, *119*, 1571–1579. https://doi.org/10.1002/2013JD020578

Olivier, J. G. J., & Berdowski, J. J. M. (2001). Global emissions sources and sinks. In J. Berdowski, R. Guicherit, & B. J. Heij (Eds.), *The Climate System*, (pp. 33–78). Lisse, The Netherlands: A. A. Balkema Publishers/Swets & Zeitlinger Publishers.

Pai, S. J., Heald, C. L., Pierce, J. R., Farina, S. C., Marais, E. A., Jimenez, J. L., et al. (2019). An evaluation of global organic aerosol schemes using airborne observations. *Atmospheric Chemistry and Physics Discussions*. https://doi.org/10.5194/acp-2019-331

Park, M., Randel, W. J., Gettelman, A., Massie, S., & Jiang, J. (2007). Transport above the Asian summer monsoon anticyclone inferred from Aura MLS tracers. *Journal of Geophysical Research*, *112*, D16309. https://doi.org/10.1029/2006JD008294

Park, R. J., Jacob, D. J., Chin, M., & Martin, R. V. (2003). Sources of carbonaceous aerosols over the United States and implications for natural visibility. *Journal of Geophysical Research*, *108*(D12), 4355. https://doi.org/10.1029/2002JD003190

Park, R. J., Jacob, D. J., Field, B. D., Yantosca, R. M., & Chin, M. (2004). Natural and transboundary pollution influences on sulfate-nitrate-ammonium aerosols in the United States: Implications for policy. *Journal of Geophysical Research*, *109*, D15204. https://doi.org/10.1029/2003JD004473

Ploeger, F., Gottschling, C., Griessbach, S., Grooß, J.-U., Guenther, G., Konopka, P., et al. (2015). A potential vorticity-based determination of the transport barrier in the Asian summer monsoon anticyclone. *Atmospheric Chemistry and Physics*, *15*, 13,145–13,159. https://doi.org/10.5194/acp-15-13145-2015

Pye, H. O. T., Chan, A. W. H., Barkley, M. P., & Seinfeld, J. H. (2010). Global modeling of organic aerosol: The importance of reactive nitrogen (NO_x and NO_3). *Atmospheric Chemistry and Physics*, *10*, 11,261–11,276. https://doi.org/10.5194/acp-10-11261-2010

Randel, W. J., & Park, M. (2006). Deep convective influence on the Asian summer monsoon anticyclone and associated tracer variability observed with AIRS. *Journal of Geophysical Research*, *111*, D12314. https://doi.org/10.1029/2005JD006490

Randel, W. J., Park, M., Emmons, L., Kinnison, D., Bernath, P., Walker, K. A., et al. (2010). Asian monsoon transport of pollution to the stratosphere. *Science*, *328*(611), 613. https://doi.org/10.1126/science.1182274

Ridley, D. A., Heald, C. L., & Prospero, J. M. (2014). What controls recent changes in African mineral dust across the Atlantic? *Atmospheric Chemistry and Physics*, *14*, 5735–5747. https://doi.org/10.5194/acp-14-5735-2014

Rienecker, M. M., Suarez, M. J., Gelaro, R., Todling, R., Bacmeister, J., Liu, E., et al. (2011). MERRA: NASA's Modern-Era Retrospective analysis for Research and Applications. *Journal of Climate*, *24*(14), 3624–3648. https://doi.org/10.1175/JCLI-D-11-00015.1

Roiger, A., H. Schlager, K. Wissmüller, H. Aufmhoff, & F. Arnold (2013). Aircraft measurements of the SO_2 distribution in the upper troposphere and lower stratosphere, presented to the SPARC SSiRC Workshop, Atlanta, GA, November

Schroder, J. C., Campuzano-Jost, P., Day, D. A., Shah, V., Larson, K., Sommers, J. M., et al. (2018). Sources and secondary production of organic aerosols in the northeastern United States during WINTER. *Journal of Geophysical Research: Atmospheres*, *123*, 7771–7796. https://doi.org/10.1029/2018JD028475

Seinfeld, J. H., & Pandis, S. N. (1998). *Atmospheric chemistry and physics from air pollution to climate change*. New York: John Wiley and Sons, Inc.

Shah, V., Jaeglé, L., Jimenez, J. L., Schroder, J. C., Campuzano-Jost, P., Campos, T. L., et al. (2019). Widespread pollution from secondary sources of organic aerosols during winter in the northeastern United States. *Geophysical Research Letters*, *46*, 2976–2983. https://doi.org/10.1029/2018GL081530

Thomason, L. W., & Vernier, J.-P. (2013). Improved SAGE II cloud/aerosol categorization and observations of the Asian Tropopause Aerosol Layer: 1989–2005. *Atmospheric Chemistry and Physics*, *13*, 4605–4616. https://doi.org/10.5194/acp-13-4605-2013

Thornton, D. C., Bandy, A. R., Blomquist, B. W., Bradshaw, J. D., & Blake, D. R. (1997). Vertical transport of sulfur dioxide and dimethyl sulfide in deep convection and its role in new particle formation. *Journal of Geophysical Research*, *102*(D23), 28,501–28,509.

Toon, O. B., Maring, H., Dibb, J., Ferrare, R., Jacob, D., Jensen, E., et al. (2016). Planning, implementation, and scientific goals of the Studies of Emissions and Atmospheric Composition, Clouds and Climate Coupling by Regional Surveys (SEAC4RS) field mission. *Journal of Geophysical Research: Atmospheres*, *121*, 4967–5009. https://doi.org/10.1002/2015JD024297

Tost, H. (2017). Chemistry–climate interactions of aerosol nitrate from lightning. *Atmospheric Chemistry and Physics*, *17*, 1125–1142. https://doi.org/10.5194/acp-17-1125-2017

Vernier, J.-P., Fairlie, T. D., Deshler, T., Venkat Ratnam, M., Gadhavi, H., Kumar, B. S., et al. (2018). BATAL: The Balloon campaigns of the Asian Tropopause Aerosol Layer. *Bulletin of the American Meteorological Society*, *2018*, 955–973.

Vernier, J.-P., Fairlie, T. D., Natarajan, M., Wienhold, F. G., Bian, J., Martinsson, B. G., et al. (2015). Increase in upper tropospheric and lower stratospheric aerosol levels and its potential connection with Asian pollution. *Journal of Geophysical Research: Atmospheres*, *120*, 1608–1619. https://doi.org/10.1002/2014JD022372

Vernier, J.-P., Thomason, L. W., & Kar, J. (2011). CALIPSO detection of an Asian Tropopause Aerosol Layer. *Geophysical Research Letters*, *38*, L07804. https://doi.org/10.1029/2010GL046614

Vogel, B., Günther, G., Müller, R., Grooß, J.-U., Afchine, A., Bozem, H., et al. (2016). Long-range transport pathways of tropospheric source gases originating in Asia into the northern lower stratosphere during the Asian monsoon season 2012. *Atmospheric Chemistry and Physics*, *16*, 15,301–15,325. https://doi.org/10.5194/acp-16-15301-2016

Vogel, B., Günther, G., Müller, R., Grooß, J.-U., & Riese, M. (2015). Impact of different Asian source regions on the composition of the Asian monsoon anticyclone and of the extratropical lowermost stratosphere. *Atmospheric Chemistry and Physics*, *15*, 13,699–13,716. https://doi.org/10.5194/acp-15-13699-2015

Wang, Q., Jacob, D. J., Fisher, J. A., Mao, J., Leibensperger, E. M., Carouge, C. C., et al. (2011). Sources of carbonaceous aerosols and deposited black carbon in the Arctic in winter-spring: Implications for radiative forcing. *Atmospheric Chemistry and Physics*, *11*, 12,453–12,473.

Wang, Y., Jacob, D. J., & Logan, J. A. (1998). Global simulation of tropospheric O_3-NO_x-hydrocarbon chemistry, 1. Model formulation. *Journal of Geophysical Research*, *103*, 10,713–10,726.

Wesely, M. L. (1989). Parameterization of surface resistance to gaseous dry deposition in regional-scale numerical models. *Atmospheric Environment*, *23*, 1293–1304.

Winker, D. M., Pelon, J., Coakley, J. A. Jr., Ackerman, S. A., Charlson, R. J., Colarco, P. R., et al. (2010). The CALIPSO mission: A global 3D view of aerosols and clouds. *Bulletin of the American Meteorological Society*, *91*(9), 1211–1230. https://doi.org/10.1175/2010BAMS3009.1

Yevich, R., & Logan, J. A. (2003). An assessment of biofuel use and burning of agricultural waste in the developing world. *Global Biogeochemical Cycles*, *17*(4), 1095. https://doi.org/10.1029/2002GB001952

Yu, K., Keller, C. A., Jacob, D. J., Molod, A. M., Eastham, S. D., & Long, M. S. (2018). Errors and improvements in the use of archived meteorological data for chemical transport modeling: An analysis using GEOS-Chem v11-01 driven by GEOS-5 meteorology. *Geoscientific Model Development*, *11*, 305–319. https://doi.org/10.5194/gmd-11-305-2018

Yu, P., Rosenlof, K. H., Liu, S., Telg, H., Thornberry, T. D., Rollins, A. W., et al. (2017). Efficient transport of tropospheric aerosol into the stratosphere via the Asian summer monsoon anticyclone. *Proceedings of the National Academy of Sciences of the USA*, *114*(27), 6972–6977. https://doi.org/10.1073/pnas.1701170114

Yu, P., Toon, O. B., Neely, R. R., Martinsson, B. G., & Brenninkmeijer, C. A. M. (2015). Composition and physical properties of the Asian Tropopause Aerosol Layer and the North American Tropospheric Aerosol Layer. *Geophysical Research Letters*, *42*, 2540–2546. https://doi.org/10.1002/2015GL063181

Zhang, Q., Streets, D. G., Carmichael, G. R., He, K. B., Huo, H., Kannari, A., et al. (2009). Asian emissions in 2006 for the NASA INTEX-B mission. *Atmospheric Chemistry and Physics*, *9*, 5131–5153.